



Stewart, P. S. (2017) Instabilities in flexible channel flow with large external pressure. *Journal of Fluid Mechanics*, 825, pp. 922-960. (doi:[10.1017/jfm.2017.404](https://doi.org/10.1017/jfm.2017.404))

This is the author's final accepted version.

There may be differences between this version and the published version. You are advised to consult the publisher's version if you wish to cite from it.

<http://eprints.gla.ac.uk/141201/>

Deposited on: 22 May 2017

Enlighten – Research publications by members of the University of Glasgow
<http://eprints.gla.ac.uk>

Instabilities in flexible channel flow with large external pressure

Peter S. Stewart

The Mathematics and Statistics Building, University of Glasgow, University Place, Glasgow.
G12 8SQ

(Received 19 May 2017)

We examine the stability of laminar high-Reynolds-number flow through an asymmetric flexible-walled channel driven by a fixed upstream flux and subject to a (large) uniform external pressure. We construct a long wavelength, spatially one-dimensional model using a flow profile assumption, modelling the flexible wall as a thin tensioned membrane subject to a large axial pre-stress. We numerically construct the non-uniform static shape of the flexible wall and consider its stability using both a global eigensolver and numerical simulation of the nonlinear governing equations. The system admits multiple static solutions, including a highly collapsed steady state where the membrane has a single constriction which increases with increasing external pressure. We demonstrate that the non-uniform static state is unstable to two distinct (infinite) families of normal modes which we characterise in the limit of large external pressure. In particular, there is a family of low-frequency oscillatory modes which each persist to low membrane tensions, where the most unstable mode has an oscillating membrane profile which is outwardly bulged at the centre of the domain with a narrow constriction at the downstream end. In addition, there is a family of high-frequency oscillatory modes which are each unstable beyond a critical value of the tension within a two-branch neutral curve. Unstable modes along the lower branch of the neutral curve are sustained by a leading-order balance between unsteady inertia and the restoring force of membrane tension along the channel. In addition, we elucidate the mechanism of energy transfer to sustain the self-excited oscillations: oscillations decrease the mean maximal constriction of the channel over a period, which reduces the overall dissipation of the mean flow and releases energy to sustain the instability. Fully nonlinear simulations indicate that as the Reynolds number increases these unstable normal modes can grow supercritically into sustained large amplitude ‘slamming’ oscillations, where the membrane is periodically drawn very close to the opposite rigid wall before recovering.

1. Introduction

In the human body there are many examples of flexible-walled vessels conveying a flow. Under certain conditions, fluid-structure interaction can promote instability which manifests as a clinically detectable (often audible) signal, such as Korotkoff noises during blood pressure measurement, wheezing in lung airways or sound production by the vocal folds; experimental and theoretical models of these flow-induced instabilities have been thoroughly reviewed elsewhere (see, for example Grotberg & Jensen 2004; Heil & Hazel 2011). Once properly understood, these physiological phenomena can be used to develop new clinical measurement devices, using the transition to instability as a detectable threshold for the system. For example, in a recent study we characterised the onset of retinal venous pulsations (RVP) in the human central retinal vein, where the flow of blood through the vein triggers spontaneous transition to a vigorous high-frequency

pulsation once the intraocular pressure (IOP, the pressure in the eye external to the vein wall) exceeds a threshold dependent on the intracranial pressure (Stewart *et al.* 2014). The predicted onset curve provides a theoretical foundation for a non-invasive method to measure the intracranial pressure for a known IOP.

In this paper we consider a theoretical model for flow through a planar (asymmetric) flexible-walled channel, devised as a two-dimensional analogue of flow through a compliant conduit in the body, first presented by Pedley (1992). In particular, the setup considered below includes rigid segments of fixed (uniform) width up and downstream of the flexible portion, as a model for Starling resistor experiments (eg. Bertram 2003; Bertram & Tscherry 2006). Models for this system vary in complexity, ranging from spatially one-dimensional models (Stewart *et al.* 2009; Xu *et al.* 2013), rational asymptotic models in the limit of large Reynolds number (Jensen & Heil 2003; Pihler-Puzović & Pedley 2013), eigenfunction expansions based on the local stability (Stewart *et al.* 2010) and full two-dimensional numerical simulations (Luo & Pedley 1996; Jensen & Heil 2003; Luo *et al.* 2008; Liu *et al.* 2009, 2012; Xu *et al.* 2014). These models exhibit a variety of oscillatory behaviour depending on how the flow is driven, which could be with either a fixed upstream pressure or a fixed upstream flux. In addition, the behaviour of the system is heavily influenced by the choice of elastic wall properties. Previous models have employed a variety of approaches, including modelling the deformation of the wall using an *ad hoc* tube law (eg Cancelli & Pedley 1985), as a pre-stressed (*ie.* tensioned) membrane (eg Luo & Pedley 1996), an elastic beam with finite bending stiffness (eg Luo *et al.* 2008) and a thin elastic shell (eg Jensen & Heil 2003). In this study we model the flexible wall as a tensioned membrane with a large pre-stress, which is assumed to dominate the other elastic restoring forces. The effects of wall mass and damping are also ignored for simplicity.

For flow driven by a prescribed upstream pressure the primary global instability for large membrane tension (so that the wall is almost flat) has been shown to be a so-called ‘sloshing’ mode driven by an asymmetry in kinetic energy flux extraction along the rigid upstream and downstream portions of the channel (Jensen & Heil 2003; Stewart *et al.* 2009, 2010). The oscillation profile of the primary global instability has a single extremum across the channel length, so is termed mode-1. This asymptotic mechanism can be generalised to three-dimensional flow through a collapsible tube with elliptical cross-section (Whittaker *et al.* 2010; Whittaker 2015).

Conversely, for flow driven by a fixed upstream flux the primary global instability of the system is typically to a so called mode-2 oscillation, where the eigenfunction is inflated at the upstream end of the compliant segment and collapsed at the downstream end (Luo & Pedley 1996; Luo *et al.* 2008). The recent one-dimensional model of Xu *et al.* (2013) (similar to that considered below), with a prescribed external pressure gradient to maintain a uniform basic state, demonstrated that for sufficiently low membrane tension the system is unstable to a family of normal modes; there exists a critical value of the membrane tension above which the uniform state is always stable. For a sufficiently long downstream rigid segment they observe saw-tooth oscillations which are also evident in numerical simulations of the full two-dimensional system (Xu *et al.* 2014). Conversely, using the same model they also demonstrate the existence of a highly collapsed static state which is always unstable to time-dependent perturbations (Xu & Jensen 2015).

In some regions of parameter space, for either fixed upstream pressure or flux, these instabilities can grow into large amplitude ‘slamming’ oscillations (Stewart *et al.* 2010; Stewart 2010; Xu *et al.* 2013), where the membrane is transiently drawn very close to the rigid wall before recovering. A simple mechanism for this behaviour was outlined by Stewart *et al.* (2010) and a detailed asymptotic description was given by Xu & Jensen

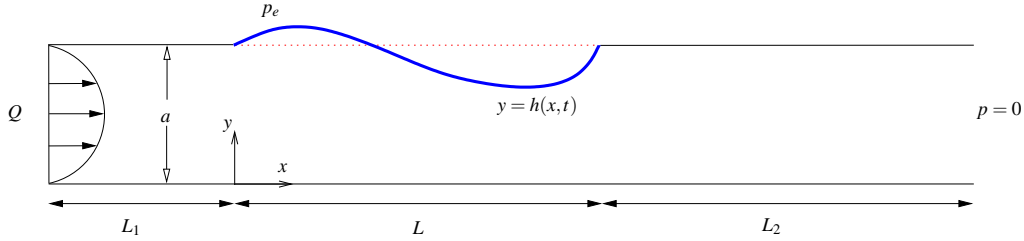


FIGURE 1. Setup of the model in dimensionless variables.

(2015). The unstable modes identified below grow into similar large-amplitude ‘slamming’ oscillations.

In this paper we revisit the one-dimensional model of Stewart *et al.* (2009) (see also Xu *et al.* 2013, 2014), to incorporate a uniform pressure on the exterior of the flexible segment of the channel (§2), driving the flow with a fixed upstream flux. This change suppresses the uniform state considered by Xu *et al.* (2013, 2014) but instead facilitates a number of non-uniform static configurations (computed in §3). We consider the linear stability of these non-uniform states to (time-dependent) perturbations using a global eigensolver (§4). As a result, we elucidate two new (infinite) families of oscillatory normal modes which we characterise in the limit of large external pressure; one family comprises low-frequency modes (described in §5), while the other consists of high-frequency modes of oscillation (described in §6). Furthermore, in §7 we conduct fully nonlinear simulations of the model, examining the nonlinear development of the primary global instability, the energy budget sustaining these instabilities. The corresponding inviscid static state of the system is discussed in appendix A. An alternative view of the neutral stability curves across the parameter space is given in appendix B. A discussion of the asymptotic structure of the low-frequency oscillations is given in appendix C.

2. The model

We consider the two-dimensional flow of an incompressible Newtonian fluid of density ρ and viscosity μ through a long (planar) rigid channel of constant width a and total length L_0 . A segment of length L of one wall of this channel is replaced by a mass-less membrane with constant longitudinal tension T_0 , forming an upstream rigid segment of length L_1 and a downstream rigid segment of length L_2 either side of the compliant segment. We measure lengths along the entirely rigid wall by the coordinate x , where $x = 0$ is the intersection between the upstream rigid segment and the flexible membrane. Similarly, we measure perpendicular displacements from the rigid wall by the coordinate y , where the position of the flexible wall is denoted as $y = h(x, t)$ across $0 \leq x \leq L$. The model setup is shown in figure 1.

Flow along the channel with velocity $\mathbf{u} = (u, v)$ and pressure p satisfies the two-dimensional Navier–Stokes equations, driven by a fixed flux Q (per unit width in the out-of-plane direction) at the upstream end and a fixed pressure P_0 at the downstream end. Furthermore, we impose a constant external pressure P_e on the flexible membrane. Neglecting normal viscous stresses (which are typically small for the parameters considered below), a normal stress balance on the wall takes the form

$$p = P_e - T_0 \kappa(h), \quad (y = h), \quad (2.1)$$

where $\kappa(h)$ represents the curvature of the elastic interface $y = h(x, t)$ (see for example Jensen & Heil 2003; Stewart *et al.* 2009).

We adopt a long-wavelength approach by rescaling the variables according to

$$x = L\hat{x}, \quad y = a\hat{y}, \quad u = (Q/a)\hat{u}, \quad v = (Q/L)\hat{v}, \quad p = P_0 + \rho(Q^2/a^2)\hat{p}, \quad (2.2)$$

where variables with a double hat are assumed $O(1)$, resulting in the following dimensionless groups

$$R = \frac{\rho Q}{\mu}, \quad p_e = \frac{a^2(P_e - P_0)}{\rho Q^2}, \quad T = \frac{aT_0}{Q^2}, \quad \hat{L}_1 = \frac{L_1}{a}, \quad \hat{L}_2 = \frac{L_2}{a}, \quad (2.3)$$

denoting the Reynolds number, the dimensionless external pressure, the dimensionless membrane tension and the dimensionless lengths of the upstream and downstream segments, respectively. We henceforth drop double hats for notational convenience.

Neglecting terms of $O(a^2/L^2)$, the flow satisfies the long-wavelength (dimensionless) Navier–Stokes equations, in the form

$$u_x + v_y = 0, \quad (2.4a)$$

$$u_t + uu_x + vv_y = -p_x + \frac{1}{R}u_{yy}, \quad (2.4b)$$

$$p_y = 0, \quad (2.4c)$$

subject to boundary conditions of no-slip along the rigid segments of the channel walls, $u = v = 0$; along the flexible membrane the flow is subject to no slip and kinematic conditions in the form

$$u = 0, \quad v = h_t, \quad (y = h), \quad (2.4d)$$

as well as continuity of normal stress (dimensionless, long-wavelength version of (2.1)),

$$p = p_e - Th_{xx}, \quad (y = h). \quad (2.4e)$$

To allow analytical progress, we reduce the governing equations to a one-dimensional system in a similar manner to other studies of collapsible channel flow (Stewart *et al.* 2009, 2010; Xu *et al.* 2013, 2014); this reduction is described in detail by Stewart *et al.* (2009). In summary, since p is independent of y through (2.4c) we integrate (2.4a) and (2.4b) across the channel width and close the resulting system of equations using a von Karman–Pohlhausen flow profile assumption, where we set

$$u = \frac{6qy(h-y)}{h^3}, \quad q = \int_0^h u \, dy, \quad (2.5)$$

where q is a flux per unit width in the out-of-plane direction. Although not strictly rational, predictions of similar models using these flow profile assumptions show encouraging agreement with full numerical simulations of the same system (Stewart *et al.* 2010; Xu *et al.* 2014).

Since the pressure does not vary in the cross-stream direction (2.4c), in the compliant segment of the channel ($0 \leq x \leq 1$) the fluid pressure follows directly from the normal stress boundary condition (2.4e). Conversely, in the rigid segments of the channel, where the fluid flux is spatially uniform ($h = 1$, $q_x = 0$), the fluid pressure varies linearly in x through (2.4b). For the upstream rigid segment ($-L_1 \leq x \leq 0$) the inlet flux condition dictates that $q = 1$ everywhere, forming a boundary condition for the compliant segment while the corresponding upstream driving pressure follows as

$$p_u(t) = p(-L_1, t) = p_e + \frac{12L_1}{R} - Th_{xx}(0, t). \quad (2.6)$$

However, since the flux is constant, consideration of flow in this segment is unnecessary

and the parameter L_1 can be set to zero without loss of generality (in agreement with Xu *et al.* 2013, 2014).

In the downstream rigid segment ($1 \leq x \leq 1 + L_2$) the x -momentum equation can be rearranged to solve for the fluid pressure profile subject to the compatibility constraint

$$Th_{xx} = p_e - L_2 \left[\frac{12q}{R} + q_t \right] \quad (x = 1), \quad (2.7)$$

which forms a boundary condition on the flow in the compliant segment ($x = 1$). The system is closed by imposing that the membrane remains pinned at its ends, so that $h(0) = h(1) = 1$.

Hence, the governing equations can be summarised as

$$h_t + q_x = 0, \quad q_t + \frac{6}{5} \left(\frac{q^2}{h} \right)_x = Thh_{xxx} - \frac{12}{R} \frac{q}{h^2}, \quad (2.8a)$$

subject to boundary conditions

$$h = 1, \quad q = 1, \quad (x = 0), \quad (2.8b)$$

$$h = 1, \quad Th_{xx} = p_e - L_2 \left(\frac{12}{R} q + q_t \right), \quad (x = 1), \quad (2.8c)$$

which forms a closed system. These governing equations are similar to those derived by Xu *et al.* (2013, 2014), although here we consider a constant external pressure as opposed to an external pressure gradient, which modifies (2.8a,c).

This system includes all the essential ingredients for predicting the onset of self-excited oscillations (fluid inertia, a source of dissipation, wall elasticity) and can be solved with much reduced computational cost compared to the full two-dimensional system. This model (2.8) converges to the full two-dimensional (long-wavelength) system in the limit as $R \rightarrow 0$ (*cf.* lubrication theory). For $R > 0$, use of the von Karman–Pohlhausen flow approximation means that this model is not entirely rational, but it remains a paradigmatic example whose behaviour can be used to better understand some aspects of what can be found in the two-dimensional system. For example, versions of these equations with an external pressure gradient (Stewart *et al.* 2009) have been able to replicate many of the features of the ‘sloshing’ oscillations found in the two-dimensional system by Jensen & Heil (2003) driven by fixed upstream pressure in the limit of large T . In addition, Xu *et al.* (2014) showed that these equations (again with an external pressure gradient) predicted a new family of ‘sawtooth’ oscillations driven by fixed upstream flux, which were also present in full two-dimensional simulations. Finally, Stewart *et al.* (2010) showed that these equations predict highly nonlinear ‘slamming’ oscillations (discussed below) in some regions of parameter space, in strong qualitative agreement with full two-dimensional computations.

2.1. Static solutions

Static solutions to (2.8) must have unit flux to satisfy the inlet flow condition, while the corresponding membrane profile $h = h^{(s)}(x)$ must satisfy the third order nonlinear ODE

$$\frac{6}{5} \left(\frac{1}{h^{(s)}} \right)_x = Th^{(s)} h_{xxx}^{(s)} - \frac{12}{R} \frac{1}{(h^{(s)})^2}, \quad (0 \leq x \leq 1), \quad (2.9a)$$

subject to three boundary conditions

$$h^{(s)} = 1, \quad (x = 0), \quad (2.9b)$$

$$h^{(s)} = 1, \quad Th_{xx}^{(s)} = p_e - \frac{12L_2}{R}, \quad (x = 1). \quad (2.9c)$$

The superscript (s) has been used throughout to denote the static solution and $p^{(s)}(x)$ denotes the corresponding static pressure profile. Following Stewart *et al.* (2009), these equations can be discretised using finite differences and solved numerically using Newton's method. Static solutions to (2.9) are described in §3 below. In a similar manner to Xu *et al.* (2013), it is also instructive to consider inviscid static solutions, discussed in appendix A. Throughout this paper we consider relatively large external pressures where the channel is collapsed for a region along its length, and we typically characterise the static solutions using the maximal channel constriction $h_m^{(s)} = \min_x(h^{(s)})$ with corresponding x position $x_m^{(s)}$.

2.2. Linear stability global eigensolver

We consider the stability of a static solution of (2.9) by considering the growth of a small perturbation to this state, writing

$$(h, q) = (h^{(s)}(x), 1) + \theta \left[(\tilde{h}(x), \tilde{q}(x))e^{\sigma t} + (\tilde{h}^*(x), \tilde{q}^*(x))e^{\sigma^* t} \right], \quad (0 \leq x \leq 1), \quad (2.10)$$

where $\theta \ll 1$ and $\tilde{h}(x; \sigma)$ and $\tilde{q}(x; \sigma)$ are functions of x and $*$ denotes a complex conjugate. Substituting into the full governing equations (2.8) and neglecting terms of $O(\theta^2)$ we obtain the linearised equations

$$\sigma \tilde{h} + \tilde{q}_x = 0, \quad (2.11a)$$

$$\sigma \tilde{q} + \frac{6}{5} \left(\frac{2\tilde{q}}{h^{(s)}} - \frac{\tilde{h}}{(h^{(s)})^2} \right)_x = Th^{(s)}\tilde{h}_{xxx} + T\tilde{h}h_{xxx}^{(s)} - \frac{12}{R} \left(\frac{\tilde{q}}{(h^{(s)})^2} - \frac{2\tilde{h}}{(h^{(s)})^3} \right), \quad (2.11b)$$

subject to linearised boundary conditions

$$\tilde{h} = 0, \quad \tilde{q} = 0, \quad (x = 0), \quad (2.11c)$$

$$\tilde{h} = 0, \quad T\tilde{h}_{xx} = -L_2 \left(\frac{12}{R}\tilde{q} + \sigma\tilde{q} \right), \quad (x = 1). \quad (2.11d)$$

Equations (2.11) constitute a global eigenvalue problem for σ and the corresponding eigenfunctions $\tilde{q}(x; \sigma)$ and $\tilde{h}(x; \sigma)$, which must be solved numerically. To form a solution to the eigenvalue problem (2.11) we construct a global eigensolver by discretising the collapsible segment of the channel x onto a uniform mesh $x_j = j\Delta x$ ($j = 0, \dots, N-1$) where $\Delta x = 1/(N-1)$. We then discretise the perturbation eigenfunctions onto this mesh by writing $\tilde{h}_j = \tilde{h}(x_j; \sigma)$ and $\tilde{q}_j = \tilde{q}(x_j; \sigma)$ ($j = 0, \dots, N-1$) and form the vector of unknown coefficients $\mathbf{a} = [\tilde{h}_0, \dots, \tilde{h}_{N-1}, \tilde{q}_0, \dots, \tilde{q}_{N-1}]^T$. By expressing spatial derivatives using second-order centred finite difference approximations, we hence express (2.11) as an eigenvalue problem in the form

$$\mathbf{M}\mathbf{a} = \sigma\mathbf{a}, \quad (2.12)$$

where \mathbf{M} is a matrix of size $2N \times 2N$. The eigenvalues (σ) and corresponding eigenvectors (\mathbf{a}) can be calculated numerically using MATLAB in a straightforward manner. For computation of the energy budget below we normalize the eigenfunction so that $\max(\Re(\tilde{q}(x; \sigma))) = 1$ unless specified otherwise. Results of the linear stability analysis

are described in §4.1-4.2. In simulations we use up to a maximum of $N = 1600$ grid points to resolve the highly constricted static shape and associated eigenfunctions. Simulations for larger N became impractical and were not deemed necessary. This global eigensolver is similar in spirit to that constructed by Luo *et al.* (2008) (see also Liu *et al.* 2009, 2012) using a finite element method and an Arnoldi algorithm for computing eigenvalues, but their two-dimensional eigensolver requires extremely large matrices and is impractical for large-scale parameter sweeps. Since the present approach is one-dimensional it has the advantage of much reduced computational cost permitting a unified overview of the parameter space.

2.3. Fully nonlinear simulations

Nonlinear, time-dependent simulations of (2.8) can be constructed using the semi-implicit finite difference method described and used previously by Stewart *et al.* (2009). In particular, we discretise spatial derivatives using fourth-order finite differences and time derivatives using first-order finite differences, representing the highest spatial derivative in each equation implicitly with all other terms treated explicitly. To capture the highly complicated ‘slamming’ oscillations described below we use an increased temporal and spatial grid in regions where the membrane gets drawn close to the rigid wall. We have also thoroughly checked for convergence of the scheme using a variety of spatial and temporal grids up to a maximum of 3000 equally spaced spatial grid points. Results of the fully nonlinear simulations are described in §7. We typically characterise the numerical simulations by considering the temporal evolution of the maximal channel constriction $h_m(t) = \min_x(h(x, t))$.

2.4. Energy budget

Following Stewart *et al.* (2009), we compute the corresponding energy budget for the flow by multiplying (2.8) by $6q/(5h)$ and integrating over the channel length and width. This energy budget can be written in the form

$$\mathcal{K} + \mathcal{E} = \mathcal{F} + \mathcal{P} - \mathcal{D}_S - \mathcal{D}_A, \quad (2.13a)$$

where

$$\mathcal{K} = \frac{3}{5} \frac{\partial}{\partial t} \left(\int_0^1 \frac{q^2}{h} dx + \int_{-L_1}^0 q^2 dx + \int_1^{1+L_2} q^2 dx \right), \quad (2.13b)$$

$$\mathcal{F} = -\frac{18}{25} \left[\frac{q^3}{h^2} \right]_{x=0}^{x=1}, \quad (2.13c)$$

$$\mathcal{P} = \frac{6}{5} p_u = \frac{6}{5} \left(p_e + \frac{12L_1}{R} - Th_{xx}(0, t) \right), \quad (2.13d)$$

$$\mathcal{E} = \frac{6}{5} \frac{\partial}{\partial t} \left(\int_0^1 (p_e h + \frac{1}{2} Th_x^2) dx \right), \quad (2.13e)$$

$$\mathcal{D}_S = \frac{72}{5R} \left(\int_0^1 \frac{q^2}{h^3} dx + \int_{-L_1}^0 q^2 dx + \int_1^{1+L_2} q^2 dx \right), \quad (2.13f)$$

$$\mathcal{D}_A = \frac{3}{25} \int_0^1 \frac{q^2 q_x}{h^2} dx. \quad (2.13g)$$

where \mathcal{K} measures the rate of change of kinetic energy, \mathcal{F} is the net kinetic energy flux extracted from the mean flow, \mathcal{P} is the rate of working of upstream pressure forces, \mathcal{E} is the rate of working of pressure forces across the membrane, \mathcal{D}_S is the rate of working

of viscous forces and \mathcal{D}_A is the additional kinetic energy flux induced by the flow profile assumption. The terms in the fully nonlinear energy budget for periodic oscillations are computed in §7.3 below. It should be noted that \mathcal{P} is proportional to the upstream pressure p_u , which can in turn be expressed in terms of the external pressure on the membrane and the membrane curvature at the upstream end of the flexible segment.

2.5. Energy budget for static solutions

For a static membrane (described in §2.1) the only non-trivial contributions to the energy budget can be expressed as (steady components denoted with a superscript (s)),

$$\mathcal{P}^{(s)} = \mathcal{D}^{(s)}, \quad (2.14)$$

where

$$\mathcal{D}^{(s)} = \frac{72}{5R} \left(\int_0^1 \frac{1}{(h^{(s)})^3} dx + L_1 + L_2 \right), \quad (2.15)$$

$$\mathcal{P}^{(s)} = \frac{6}{5} \left(p_e + \frac{12L_1}{R} - Th_{xx}^{(s)}(0) \right). \quad (2.16)$$

Using the downstream boundary condition (2.9c) this static energy balance can be rewritten as

$$T \left[h_{xx}^{(s)} \right]_0^1 = \frac{12}{R} \int_0^1 \frac{1}{(h^{(s)})^3} dx; \quad (2.17)$$

this relation is employed to close the reduced system of equations constructed in the limit of large p_e in §6 below.

2.6. Rate of working of viscous dissipation

To elucidate the energy budget of neutrally stable oscillations, we consider the rate of working of viscous forces (2.13f) in more detail. In particular, we consider the time average over a period of oscillation, denoted by an overbar. We consider the perturbation expansion posed in (2.10) continued to the next order in θ in the form,

$$\begin{aligned} (h, q) = & (h^{(s)}, 1) + \theta \left[(\tilde{h}, \tilde{q})e^{\sigma t} + (\tilde{h}^*, \tilde{q}^*)e^{\sigma^* t} \right] + \\ & \theta^2 \left[(\check{h}, \check{q})e^{2\sigma t} + (\bar{h}, \bar{q}) + (\check{h}^*, \check{q}^*)e^{2\sigma^* t} \right] + O(\theta^3). \end{aligned} \quad (2.18)$$

Using this expansion we approximate \mathcal{D}_S (2.13f) by expanding in powers of θ . At leading-order $\overline{\mathcal{D}_S} = \mathcal{D}_S^{(s)}$. At the following order, the variables have components which are proportional to either $\exp(\sigma t)$ or $\exp(\sigma^* t)$, so taking the time average over a period of neutrally stable oscillation ($\Re(\sigma) = 0$) implies that the $O(\theta)$ contribution to $\overline{\mathcal{D}_S}$ must be zero. Conversely, at $O(\theta^2)$, the checked variables consist of time independent terms (denoted as \bar{h} and \bar{q} for h and q , respectively) as well as time-dependent components which are proportional to either $\exp(2\sigma t)$ or $\exp(2\sigma^* t)$. Hence, when averaging over a period of neutrally stable oscillation, we obtain a non-trivial contribution to the energy budget at $O(\theta^2)$. A similar approach was previously considered by Stewart *et al.* (2010) to compute the perturbation energy budget of ‘sloshing’ oscillations driven by fixed upstream pressure.

Hence, we expand the time-averaged rate of working of viscous dissipation in the form,

$$\overline{\mathcal{D}_S} = \mathcal{D}_S^{(s)} + \theta^2 \left(\overline{\mathcal{D}_S} + \overline{\mathcal{D}_S} \right) + O(\theta^3), \quad (2.19)$$

where

$$\overline{\mathcal{D}}_S = \frac{144}{5R} \left(\int_0^1 \frac{6\tilde{h}\tilde{h}^* - 3h^{(s)}\tilde{h}^*\tilde{q} - 3h^{(s)}\tilde{h}\tilde{q}^* + (h^{(s)})^2\tilde{q}\tilde{q}^*}{(h^{(s)})^5} dx + L_2\tilde{q}(1)\tilde{q}^*(1) \right), \quad (2.20)$$

consists of terms which involve the eigenfunctions \tilde{h} and \tilde{q} (and their complex conjugates) determined above, while

$$\overline{\mathcal{D}}_S = \frac{72}{5R} \int_0^1 \frac{-3\tilde{h}}{(h^{(s)})^4} dx \quad (2.21)$$

consists only of time-independent terms arising at second order in θ . We note that \tilde{q} must be zero to satisfy conservation of mass over a period of neutrally stable oscillation, so $\overline{\mathcal{D}}_S$ depends on \tilde{h} alone. The quantity $\overline{\mathcal{D}}_S$ can be easily computed from eigenfunctions obtained from the global stability eigensolver discussed in §2.2 above. However, solution of the $O(\theta^2)$ perturbation problem would be required to compute $\overline{\mathcal{D}}_S$, which is not considered here. We use this decomposition of $\overline{\mathcal{D}}_S$ in §7.3 below to elucidate the mechanism of energy transfer sustaining the self-excited oscillations.

3. Static membrane profiles

In this section we consider nonlinear static solutions of (2.9), summarised in figure 2. In particular, we consider a parametric plot of the minimal channel width ($h_m^{(s)} \leq 1$) as a function of the membrane tension T for several values of the Reynolds number R for fixed external pressure $p_e = 10$ and downstream length $L_2 = 3$ (figure 2a). Corresponding static membrane profiles for $T = 1$ are shown for both $R = 10$ and $R = 100$ in figure 2(b) (at the points labelled with open circles in figure 2a). Similarly, the three possible static membrane profiles for $T = 3$ and $R = 200$ are shown in figure 2(c) (at the points labelled with crosses in figure 2a). For low tensions the channel is highly constricted at one point along its length due to the collapsing influence of the external pressure (figure 2b). This collapse is further exaggerated by the Bernoulli effect as the Reynolds number increases (figure 2b). This state is similar to the highly collapsed membrane profiles reported by Xu & Jensen (2015). As the membrane tension increases the channel gradually becomes less collapsed, approaching a state where the channel is close to uniform along its length, similar to the uniform state admissible with an external pressure gradient (Xu *et al.* 2013). For low Reynolds numbers the transition between the highly collapsed and uniform states is monotonic (see curves for $R = 10$, $R = 50$ in figure 2a). However, beyond a critical Reynolds number R_b the trace of the maximal channel constriction becomes multi-valued for a range of membrane tension, exhibiting three static states for a given T (see curves for $R = 100$ and greater in figure 2a). The highly collapsed static state and the almost uniform static state are both stable to (static) perturbations, while the intermediate state is unstable. The change in stability occurs through two limit point (or saddle-node) bifurcations, one at each end the intermediate branch. The path of these limit points in parameter space is also shown as dotted lines in figures 4(a,b) and 10(a) below. Also, in figure 4(b) below we illustrate the regions of the parameter space where two stable static solutions coexist (dark shaded region). The corresponding trace of the inviscid static state (discussed in appendix A) is also shown in figure 2(a) (dashed line), where the system exhibits a single limit point (saddle-node) bifurcation at $T = T_c$ ($T_c \approx 2.426$ for $p_e = 10$), with two branches of static solutions for $T > T_c$, where the upper branch is stable and the lower branch unstable. These branches are analogous to the almost uniform and the intermediate branches identified for finite R . However, the highly collapsed static state

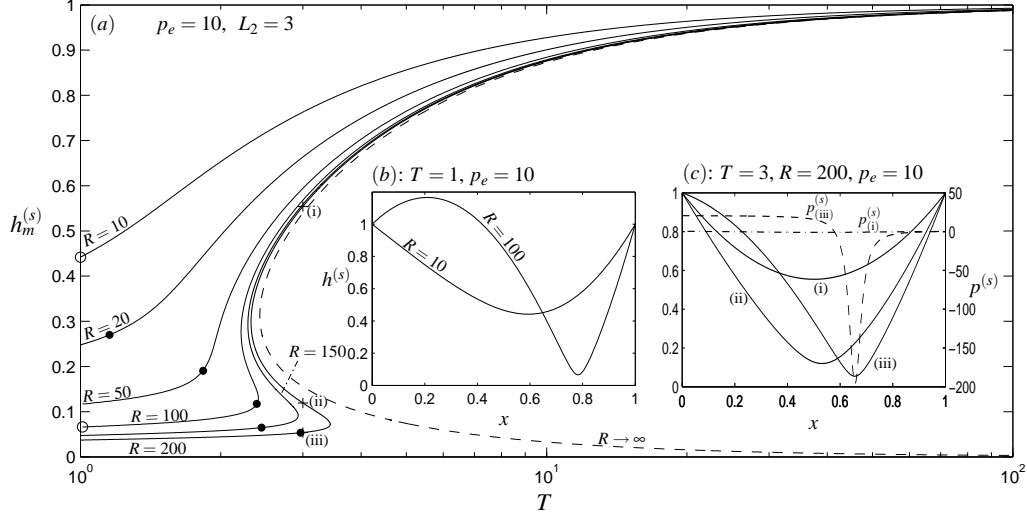


FIGURE 2. Nonlinear static solutions of the model for prescribed upstream flux: (a) plot of the maximal channel constriction as a function of the wall tension for $R = 10$, $R = 50$, $R = 100$, $R = 150$ and $R = 200$; (b) the unique static wall profiles for $T = 1$ and both $R = 10$ and $R = 100$ (points marked with open circles on (a)); (c) the three static walls profile for $T = 3$ and $R = 200$ at the points (i)-(iii) marked with crosses on (a) (left hand axis) while the corresponding static pressure profiles in (i) and (iii) are shown as a dot-dashed and dashed lines, respectively (right hand axis). Here $p_e = 10$ and $L_2 = 3$. The dashed line in (a) is the inviscid static state. The filled circles in (a) indicate the critical value of the membrane tension below which the static branch is unstable to oscillations.

for finite R does not exist in the inviscid limit, as this is maintained by viscous effects (see §6 below).

An example of the multiple static states at the same point in parameter space is shown in figure 2(c) for $T = 3$ and $R = 200$. These profiles are labelled (i)-(iii), where (i) is the most inflated profile and (iii) is the most constricted. Both (i) and (iii) are stable to (static) perturbations. This existence of multiple stable static states is reminiscent of the work of Reyn (1987) and consistent with examples of ‘flow limitation’ or ‘choking’ (Luo & Pedley 2000; Stewart 2010). Furthermore, there is a sharp contrast between the pressure profiles of these two (stable) static configurations, also shown in figure 2(c). The pressure corresponding to profile (i) (dot-dashed line in figure 2c) exhibits only small variations along the collapsible segment. Conversely, the pressure corresponding to profile (iii) (dashed line in figure 2c) is approximately piecewise constant with a decrease across the point of maximal constriction (due to viscous effects) with a significant overshoot due to the Bernoulli effect (the pressure required to maintain the rapid flow through the constriction). Siviglia & Toffolon (2014) analysed a one-dimensional model of flow in a long collapsible tube in the absence of membrane tension, showing that a localised change in the properties of the wall (mimicking our compliant segment of the channel) can induce multiple stable states, one supercritical and another which exhibits an elastic jump (and hence sharp changes in pressure), similar to the experiments of Kececioglu *et al.* (1981). Our profiles (i) and (iii) are significantly different to each other, in agreement with Siviglia & Toffolon’s results, but given the dispersive nature of the current one-dimensional model it is not clear if profile (iii) is transcritical.

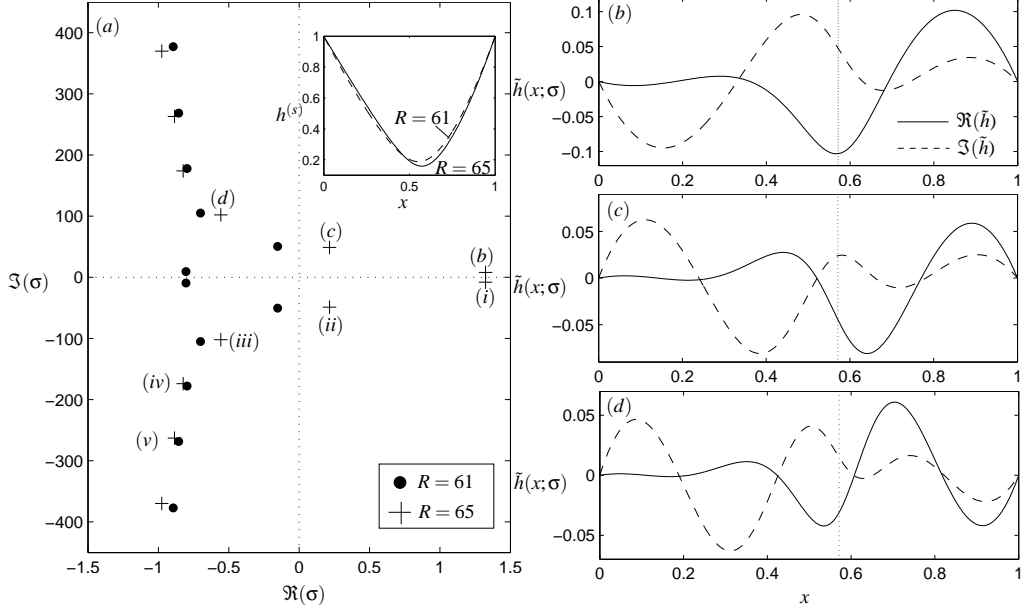


FIGURE 3. (a) Eigenvalue spectra for $T = 2$, $p_e = 10$ and $L_2 = 3$, with $R = 61$ (filled circles) and $R = 65$ (crosses). The pairs of modes are labelled (i)-(vi) in order of increasing stability. Inset shows the corresponding static shape of the wall for $R = 61$ (dashed) and $R = 65$ (solid). Corresponding eigenfunctions $\tilde{h}(x; \sigma)$ of the three most unstable modes for $R = 65$: (b) mode (i); (c) mode (ii); (d) mode (iii). Eigenfunctions have been normalised so that $\max(\Re(\tilde{q})) = 1$. The dotted line in (b-d) denotes the position $x_m^{(s)}$.

4. Linear stability of the static membrane profiles

In this section we consider the stability of the nonlinear static profiles constructed in §3, examining the structure of a typical global eigenvalue spectrum (§4.1) and isolating neutrally stable oscillatory modes (§4.2).

4.1. Typical eigenvalue spectra

Having characterised the static membrane profiles, we now use the global eigensolver described in §2.2 to consider their stability to time-dependent perturbations. Two typical eigenvalue spectra are plotted in figure 3(a), plotting $\Re(\sigma)$ against $\Im(\sigma)$ for the static state plotted in the inset. Eigenvalues appear as complex conjugate pairs, which are all stable ($\Re(\sigma) < 0$) for sufficiently small Reynolds numbers. As the Reynolds number increases a pair of eigenvalues will cross the $\Re(\sigma)$ axis with non-zero imaginary part, indicative of a Hopf bifurcation. Two cases are illustrated for $T = 2$, $p_e = 10$ and $L_2 = 3$ in figure 3(a), $R = 61$ where all eigenvalues are stable (filled black circles) and $R = 65$ where two conjugate pairs of eigenvalues are unstable (crosses). In figure 3(b-d) we plot the corresponding eigenfunctions $\tilde{h}(x, \sigma)$ of the three most unstable modes for $R = 65$; the structure of these eigenfunctions is explained in more detail below.

4.2. Neutrally stable oscillations

Neutral stability curves (along which $\Re(\sigma) = 0$) in the parameter space spanned by the membrane tension and critical Reynolds number are shown in figure 4(a) for $p_e = 10$ and $L_2 = 3$. In particular, we illustrate the neutral stability curves for the five most unstable modes identified in the spectrum in figure 3. These modes are labelled (i) to

(v). We have verified that for these parameter values the primary global instability of the system is always either to the mode labelled (i) or (iia). It should be noted that the mode labelled (ii) becomes unstable in two separate regions across the parameter space, labelled (iia) and (iib), respectively. Interestingly, the neutral curve for mode (iib) exhibits a low-frequency oscillation for low tensions (consistent with the framework described in §5) but a high-frequency oscillation for large tensions (consistent with the framework described in §6). Although these neutral curves intersect one another, they do so with distinct frequencies so there is no mode interaction. In addition, in figure 4(b) we illustrate regions of parameter space where the system is unstable to oscillations using hatching, as well as highlighting the corresponding regions of parameter space where multiple steady states exist (dark shaded region). The corresponding oscillation frequency of each mode is shown in figure 4(c); for each mode the oscillation frequency increases with membrane tension which is exploited in §6 below.

Previous studies of collapsible channel flow (eg. Luo *et al.* 2008; Stewart *et al.* 2009) characterise these modes by the number of turning points in the eigenfunction of the membrane shape, $\tilde{h}(x; \sigma)$. Hence, according to this convention for $T = 2$ the mode labelled (i) would be mode-4, the mode labelled (iia) would be mode-5 and the mode labelled (iii) would be mode-6. However, for lower tensions the mode labelled (i) has two extrema (see figure 7(a,i)) and is thus mode-2, so the shape of the eigenfunction changes along the neutral curve. In this study it emerges that for large tensions a more convenient labeling convention is to characterise the eigenfunction relative to the point of greatest channel constriction, $x_m^{(s)}$ (position denoted with a dotted line on the panels in figure 3b-d). We characterise the eigenfunctions of neutrally stable modes in more detail using the asymptotic model of §6 below.

It is also instructive to consider the onset of instability in terms of the corresponding static configuration of the membrane. In figure 2(a) we indicate with a filled circle the critical value of the membrane tension below which each branch of static solutions becomes unstable to self-excited oscillations. For this value of the external pressure, configurations approaching the uniform state (along the upper branch as $T \rightarrow \infty$) are always stable for large tensions. This is consistent with the study of Xu *et al.* (2013), who found that the uniform static configuration (maintained with an external pressure gradient) is always stable beyond a critical value of the membrane tension $T \approx 0.121$.

Of most pertinent interest in the system is the first onset of self-excited oscillations, termed the primary oscillatory instability. For increasing T , the system exhibits three distinct behaviors. Each of these is now discussed in turn.

4.2.1. Primary oscillatory instability for low membrane tensions

For sufficiently low membrane tensions the primary oscillatory instability of the system is via the mode labelled (i), as shown in figure 4. The neutral curve for this branch extends as $T \rightarrow 0$ (a singular limit) where the critical Reynolds number approaches a constant. The eigenfunction for \tilde{h} has two extrema for $T = 0.1$ and is thus mode-2 (see also plots for $T = 0.01$ in figure 7(a,iii) below). The corresponding shape of the static membrane and perturbation eigenfunction as well as the critical Reynolds number required for the onset of instability are explored in the limit as $p_e \rightarrow \infty$ in §5 and appendix C below. For larger Reynolds numbers the system admits a secondary instability of the static shape with neutral curve labelled (iib), which again persists as $T \rightarrow 0$, where the eigenfunction for \tilde{h} has three extrema for $T = 0.1$ and is thus mode-3. We further explore this family of oscillations in the limit as $T \rightarrow 0$ in §5 below, where we hypothesise that these are the first two branches of an infinite family of low-frequency oscillatory modes. The nonlinear

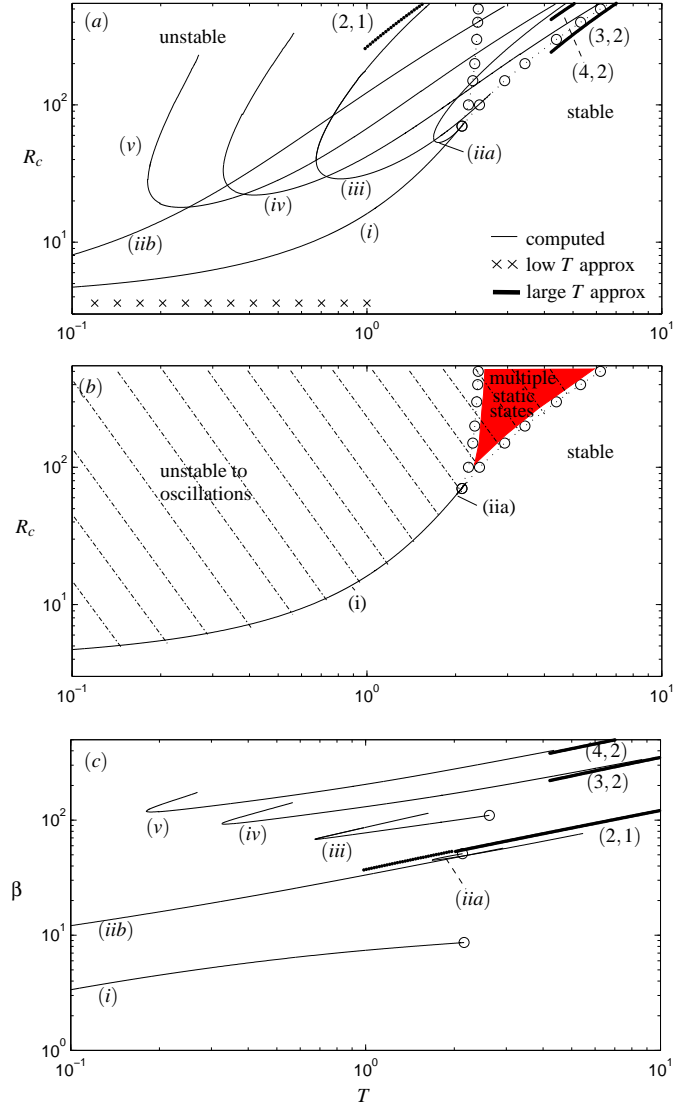


FIGURE 4. Neutrally stable modes for $p_e = 10$ and $L_2 = 3$ as a function of the membrane tension T : (a) the critical value of the Reynolds number for instability of the six most unstable modes labelled (i) to (v); (b) regions of the (T, R) parameter space where the system has multiple coexisting static states (dark shaded region) and regions where the highly collapsed basic state is unstable to oscillations (hatching) (c) corresponding frequency of the neutrally stable modes. The open circles in (a) correspond to limit (saddle) points associated with a change in the number of static configurations, while the crosses represent the leading-order prediction for the critical Reynolds number from the low-frequency theory in §5. The labels (m, n) follow from the asymptotic description of the eigenfunction of the wall shape in the limit of large T described in §6, where m is the number of turning points upstream of the constriction and n is the number of turning points downstream.

growth of oscillations along the branch (i) is explored in §7.1, while the corresponding energy budget of the fully developed oscillations is explored in §7.3.

4.2.2. Primary global instability for intermediate membrane tensions

For intermediate membrane tensions the primary oscillatory instability of the system is via the high-frequency mode labelled (iia). In this case the neutral curve does not persist to low tensions and instead takes the form of a tongue (figure 4) with an upper and lower branch (similar to other phenomena in hydrodynamic stability theory, such as the onset of Tollmien–Schlichting waves (Drazin & Reid 1981)). These tongues are similar to those found in flux-driven instabilities through a flexible walled channel elucidated by Luo *et al.* (2008), where for smaller external pressures (so the channel is less collapsed), these modes could result in small pockets of parameter space where the system is stable, surrounded by regions where it is unstable.

For larger Reynolds numbers the system admits higher modes of high-frequency instability which also arise as two branch tongues (see branches (iii), (iv) and (v) in figure 4). We hypothesise that these are the first branches of an infinite family of high-frequency oscillatory normal modes, explored in detail in §6.

As the membrane tension becomes large, the critical Reynolds number along the lower branch of the neutral curves grows proportional to T (figure 4a) and the corresponding oscillation frequencies grow proportional to $T^{1/2}$ (figure 4c). We exploit this scaling in §6 below. This high-frequency scaling is similar to the ‘sloshing’ mode identified by Jensen & Heil (2003) for instabilities driven by fixed upstream pressure, but it emerges below that the dynamics of unstable modes and the scaling of the critical Reynolds number are very different. It should be noted that neutral curves that terminate in an open circle exhibit a global bifurcation at this point (see §4.2.3 below) while those that do not persist beyond that illustrated here, but it became extremely difficult to track the neutral curve further as the static channel becomes very strongly constricted ($h_m^{(s)} \leq 0.01$), requiring a prohibitively large number of grid points to resolve the sharp gradients in the membrane profile. It is expected that a similar asymptotic framework could be constructed to describe the scalings along the upper branch of the neutral curves (where $x_m^{(s)} \rightarrow 1$), although this branch is not pertinent for the onset of instability and so is not considered here.

4.2.3. Primary global instability for large membrane tensions

As the membrane tension increases each oscillatory neutral curve (associated with a Hopf bifurcation, figure 4) eventually intersects the line of limit points associated with loss of existence of the highly collapsed static state (dotted line in figure 4), generating a co-dimension 2 bifurcation at the intersection point and suggesting that there is a homoclinic orbit in the neighbourhood of this point (Glendinning 1994). Beyond this global bifurcation point the oscillatory neutral curve terminates. Such homoclinic bifurcations are often associated with chaotic behaviour, consistent with the ‘slamming’ oscillations found in §7.2. Similar Hopf/limit-point interactions were found by Armitstead *et al.* (1996) in a lumped parameter model of self-excited oscillations in collapsible tubes.

To show this in more detail, figure 5 illustrates the neutral curves for branches (i), (iia) and (iii) and corresponding lines of limit points in the vicinity of the global bifurcation points for three cases $p_e = 10$, $p_e = 50$ and $p_e = 100$. In all cases tested the neutral curves for branches (i) and (iia) terminate extremely close to the coalescence of the two lines of limit points, but do not seem (as far as can be determined numerically) to intersect this point.

As $p_e \rightarrow \infty$, the value of T at the point of intersection of the two lines of limit points

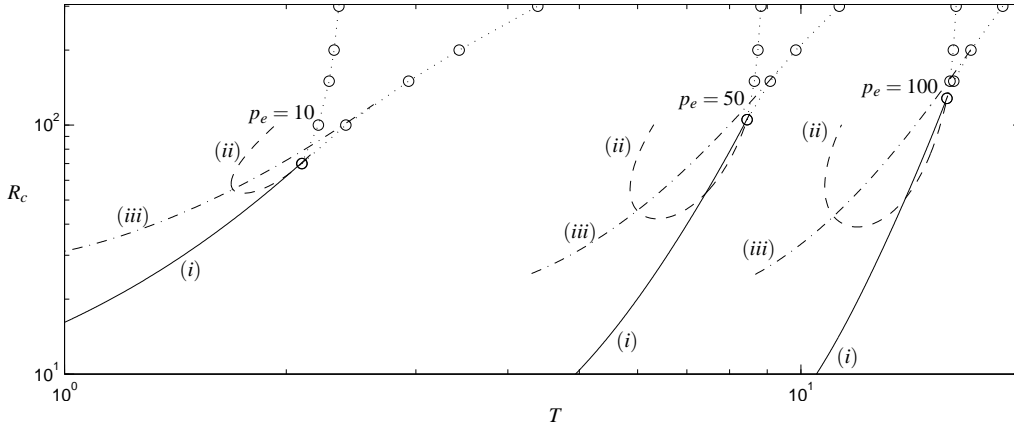


FIGURE 5. Neutral stability curves for the three most unstable modes for fixed external pressure $p_e = 10$, $p_e = 50$ and $p_e = 100$ with $L_2 = 3$: (a) the critical Reynolds number as a function of the membrane tension; (b) the corresponding oscillation frequency as a function of the membrane tension. The solid lines corresponds to mode (i), the dashed line corresponds to mode (ii) and the dot-dashed line corresponds to mode (iii). The open circles connected by dotted lines represent the line of limit (saddle) points associated with a change in the number of static configurations.

(associated with a change in the number of static configurations) approaches T_c while the corresponding Reynolds number $R \rightarrow \infty$ (figure 5), the limit point associated with the existence of the inviscid static state (appendix A). Since the neutral curves for modes (i) and (ii) always emerge very close to this intersection point, it seems that the inviscid static state is an organising centre of the dynamical system, as previously predicted by Xu *et al.* (2013) in a similar system but with an external pressure gradient.

In the region below and to the right of the co-dimension-2 points in the (T, R) parameter space (figure 4) there is only one stable static configuration. However, for larger Reynolds numbers, inside the region where two static states coexist, the modes (i), (ii) all still exist and are linearly unstable. Hence, the higher modes ((iii), (iv), \dots) are never the primary global instability of the system. The fully nonlinear behaviour in this region is explored in §7.2 below.

An alternative view of parameter space with T/p_e held fixed is considered in appendix B.

5. Low-frequency oscillations as $p_e \rightarrow \infty$

To better understand the primary oscillatory instability of the system for low membrane tensions, in figure 6(a) we illustrate the critical Reynolds number onset as a function of external pressure p_e for four fixed values of T (showing $T = 0.01$, $T = 0.1$, $T = 0.05$ and $T = 1$), with the corresponding oscillation frequency shown in figure 6(b); in this case the system is unstable above and to the right of the neutral curves. For large p_e ($p_e \gtrsim 200$) we observe that the critical Reynolds number for instability decreases proportional to p_e^{-1} (figure 6a), while the critical frequency decreases proportional to $p_e^{-1/2}$ (figure 6b). It should be noted that the primary oscillatory branch for $T = 1$ undergoes a resonant interaction with another mode, resulting in a mode coalescence and a cusp in the neutral curve in this parameter space, although the corresponding oscillation frequency changes smoothly. It emerges from the asymptotic analysis of appendix C that the leading-order Reynolds number takes the exceedingly simple form $R_c \approx 12L_2/p_e$ as

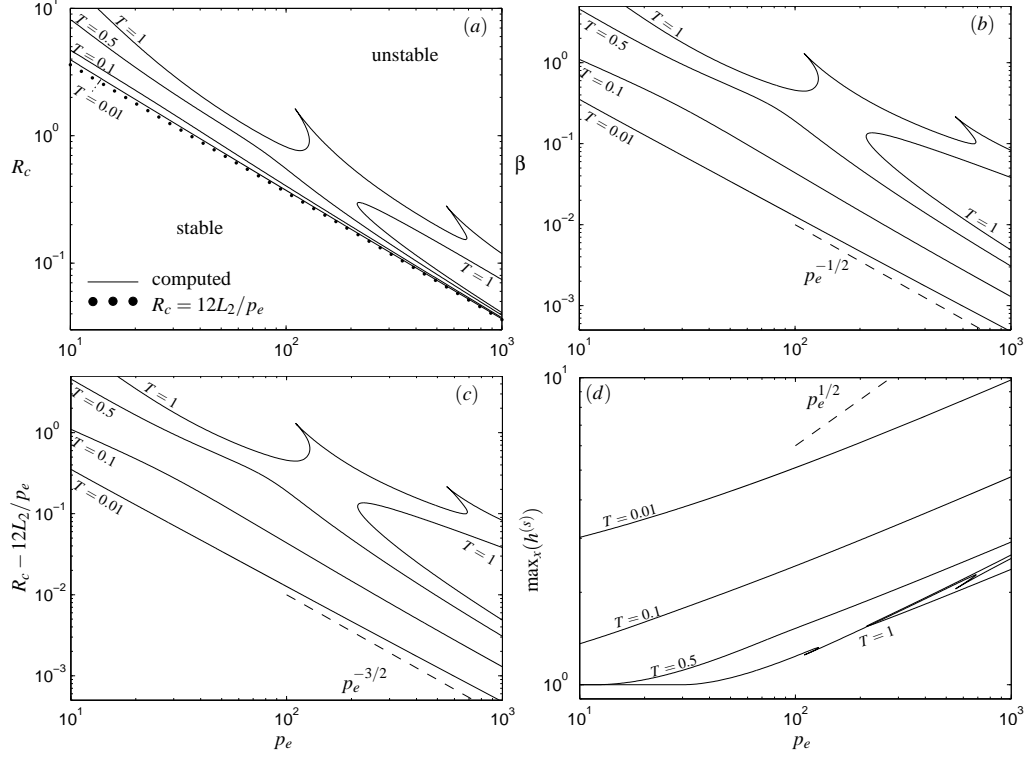


FIGURE 6. Neutral stability curves for the primary global instability for fixed tension $T = 0.01$, $T = 0.1$, $T = 0.5$ and $T = 1.0$ for $L_2 = 3$: (a) the critical Reynolds number for primary global instability as a function of the external pressure; (b) the corresponding mode frequency as a function of external pressure; (c) the difference between the computed critical Reynolds number and the leading-order constraint $R_c = 12L_2/p_e$ as a function of external pressure; (d) the maximal expansion of the channel as a function of external pressure. The filled circles in (a) represents the asymptotic result $R_c \approx 12L_2/p_e$. In all cases the neutral curve for $T = 1$ is in two pieces which may be connected for larger external pressures. The dashed line in (b) is parallel to $p_e^{-1/2}$, the dashed line in (c) is parallel to $p_e^{-3/2}$ and the dashed line in (d) is parallel to $p_e^{1/2}$.

$p_e \rightarrow \infty$, plotted as filled circles on figure 6(a), showing excellent agreement with the numerical predictions. This serves as an estimate of the critical Reynolds number for the onset of instability as $T \rightarrow 0$ for fixed p_e , plotted as crosses on figure 4(a) and showing good agreement with the numerical simulations. The membrane tension is sufficiently weak relative to p_e , so that in the steady state we are effectively imposing boundary conditions on both p_e and flux at the upstream end of the downstream segment, which produces this strong constraint on Reynolds number. In addition, to estimate the size of the first correction to the critical Reynolds number, we plot $R_c - 12L_2/p_e$ as a function of p_e (figure 6c), which decreases as $p_e^{-3/2}$.

The shape of the static membrane at criticality for $p_e = 1000$ and $T = 0.01$ is shown as the solid line in figure 7(a,i), which is significantly bulged outwards in the centre of the domain with a narrow (slightly) collapsed region at the downstream end. To quantify this bulged state we trace the maximal membrane deflection as a function of external pressure in figure 6(d) for the four values of T considered in figure 6. In all cases the maximal deflection increases with p_e , but the scaling behaviour is more difficult to estimate as the maximal membrane deflection and the position of that maximum are both changing.

We plot the perturbation eigenfunction for $T = 0.01$ at $p_e = 1000$ in figure 7, showing the real and imaginary parts of \tilde{q} (figure 7(a,ii)) and \tilde{h} (figure 7(a,iii)). In this case the static wall shape has two extrema (mode-2), as has the corresponding perturbation membrane shape. This is consistent with previous studies of collapsible channel flow driven by a fixed upstream flux (Luo & Pedley 1996; Xu *et al.* 2013).

Using these observations, in appendix C we construct an asymptotic framework in the limit $p_e \rightarrow \infty$ for the leading-order profiles of the static membrane shape and the corresponding perturbation eigenfunction. Each profile is divided into two regions, a core region across the interior of the domain (region 1) and a narrow boundary layer of thickness $p_e^{-1/2}$ at the downstream end (region 2). These approximations are plotted against their numerically computed equivalents in figure 7(a,ii) and (a,iii), showing good qualitative agreement. We do not, however, use this asymptotic framework to construct the critical conditions for instability as $p_e \rightarrow \infty$, since this requires expansion of both the static and perturbation profiles to higher orders, where the equations in each region must be solved numerically.

In a similar spirit to that described above, Stewart *et al.* (2009) used the present one-dimensional model with an external pressure gradient to describe the nonlinear stability of a mode-2 buckled configuration and the corresponding energy budget of oscillations. However, this study was for flow driven by a fixed upstream pressure and mechanisms of energy transfer are not comparable to the present case.

6. High-frequency oscillations as $p_e \rightarrow \infty$

Close to the region of parameter space with two stable static states, the high-frequency mode labelled (ii) becomes more unstable than mode (i) and is the primary oscillatory instability of the system. The region of parameter space where this mode is dominant becomes larger as $p_e \rightarrow \infty$ (see figure 5). This mode becomes unstable through a two branch neutral curve, as illustrated in figure 4. The asymptotic structure of modes along the lower branch of this neutral curve is described in this section.

Following the observed scaling of the neutral curves for large T , R and p_e (figures 4, 10) we construct an asymptotic approximation to the highly collapsed static state and the corresponding oscillatory profiles in the limit of large external pressure. We rescale

$$T = p_e \hat{T}, \quad R = p_e \hat{R}, \quad \sigma = p_e^{1/2} \hat{\sigma}, \quad (6.1)$$

where hatted quantities are assumed $O(1)$. It should be noted that Xu & Jensen (2015) also considered the stability of a highly constricted membrane profile using the same one-dimensional model but with an external pressure gradient. They found that the highly collapsed state is always unstable to perturbations and so they could not construct the neutral curves. Instead, they elucidated the dynamics of nonlinear ‘slamming’ motion in a slightly different dominant balance with $\sigma = O(1)$ and $L_2 \gg 1$ but using a three region decomposition very similar to that considered below.

In what follows, similar to figure 10 below, we consider \hat{T} and L_2 to be input parameters and look for the critical values of the Reynolds number $\hat{R} = \hat{R}_c$ and the corresponding critical frequency $\Im(\hat{\sigma}) = \hat{\beta}$ for neutral stability.

Three typical static membrane profiles for modes that persist to large membrane tensions are shown in figure 7 for mode (iv) (figure 7(b,i)), mode (v) (figure 7(c,i)) and mode (iib) (figure 7(d,i)). The corresponding perturbation eigenfunctions for \tilde{q} are shown in figures 7(b,ii), (c,ii) and (d,ii) and \tilde{h} are shown in figures 7(b,iii), (c,iii) and (d,iii). In all cases the magnitude of the real parts of \tilde{q} are significantly greater than the imaginary part (with an exception noted below), so we assume \tilde{q} is purely real to leading-order. In

a similar manner, it then follows that at neutral stability \tilde{h} must be purely imaginary to leading-order.

Following Xu & Jensen (2015) we decompose the membrane profile into three asymptotic regions. We denote the asymptotic approximation to the point of maximal constriction as x_0 (determined in §6.5 below as part of the solution), we denote region 1 as upstream of this constriction ($0 \leq x \leq x_0$, discussed in §6.1), region 2 as downstream of the constriction ($x_0 \leq x \leq 1$, discussed in §6.2) and Region 3 as local to this constriction ($x \sim x_0$, discussed in §6.3). We consider the scalings for each region in turn. In this section we denote parameters and dependent variables in the asymptotic problems with a hat, to distinguish from their equivalents in the full problem, and a numbered subscript to denote the region where that variable is defined.

We use this asymptotic approach to approximate the static solutions for a given \hat{R} (§6.4) and then examine its stability by constructing the neutral oscillation frequency and corresponding point of maximal constriction (§6.5), the corresponding neutral stability curves (§6.6) and the outer approximation to the perturbation eigenfunction (§6.7).

6.1. Region 1

To compute an approximation to the static membrane shape in region 1 ($0 \leq x \leq x_0$, denoted with the subscript 1), we expand the static membrane profile according to

$$h^{(s)} = \hat{h}_1^{(s)} + O(p_e^{-1/2}). \quad (6.2)$$

In region 1 the leading-order static governing equations (2.9) become

$$\hat{h}_{1,xxx}^{(s)} = 0, \quad (0 \leq x \leq x_0), \quad (6.3a)$$

subject to boundary conditions,

$$\hat{h}_1^{(s)}(0) = 1, \quad \hat{h}_1^{(s)}(x_0) = 0. \quad (6.3b)$$

This system can be solved to obtain

$$\hat{h}_1^{(s)} = \frac{1}{2}\bar{A}_1 x(x - x_0) + \frac{x_0 - x}{x_0}, \quad (x_0 \leq x \leq 1), \quad (6.3c)$$

where \bar{A}_1 is a constant which is determined by matching into region 3.

Similarly, to construct an approximation to the perturbation eigenfunction across region 1 we expand the dependent variables according to

$$\tilde{h} = p_e^{-1/2}\hat{h}_1 + O(p_e^{-1}), \quad (6.4a)$$

$$\tilde{q} = \hat{q}_1 + O(p_e^{-1/2}). \quad (6.4b)$$

To leading-order across region 1 the linearised governing equations (2.11) can be written entirely in terms of \hat{q}_1 in the form,

$$\hat{\sigma}^2 \hat{q}_1 + \hat{T} \hat{h}_1^{(s)} \hat{q}_{1,xxxx} = 0, \quad (0 \leq x \leq x_0), \quad (6.5a)$$

subject to boundary conditions

$$\hat{q}_1 = 0, \quad \hat{q}_{1,x} = 0, \quad (x = 0), \quad (6.5b)$$

$$\hat{q}_1 = 0, \quad \hat{q}_{1,x} = 0, \quad (x = x_0). \quad (6.5c)$$

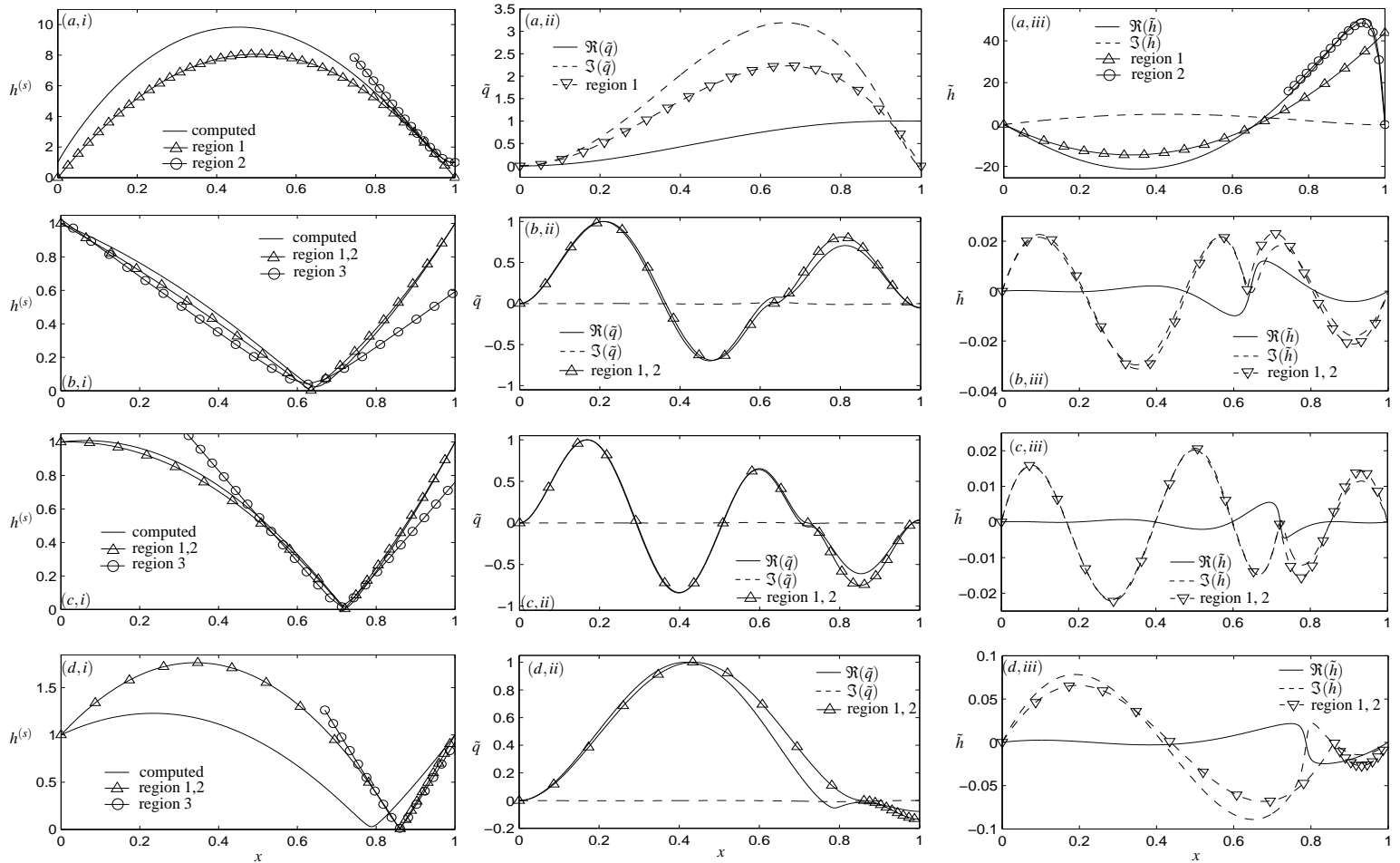


FIGURE 7. Static membrane profiles (panel (\cdot ,i)) and the real and imaginary parts of the corresponding perturbation eigenfunctions \tilde{q} (panel (\cdot ,ii)) and \tilde{h} (panel (\cdot ,iii)) at neutral stability for $L_2 = 3$, showing (a, \cdot) mode (i) for $T = 0.01$, $p_e = 1000$, $R_c \approx 0.03648$; (b, \cdot) mode (iv) for $T = 10$, $p_e = 50$, $R_c \approx 338.44$; (c, \cdot) mode (v) for $T = 10$, $p_e = 50$, $R_c \approx 677.65$; (d, \cdot) mode (iib) for $T = 2$, $p_e = 10$, $R_c \approx 320.09$. The symbols on each panel denote the corresponding predictions of the asymptotic approximation in the limit of large p_e for both low-frequency modes (panel a) and high-frequency modes (panels b-d).

This represents a leading-order balance between the unsteady inertial forces and the restoring force of membrane tension. It should be noted that only $\hat{\sigma}^2$ appears in the governing equations. Hence, at neutral stability ($\hat{\sigma} = i\hat{\beta}$) the equations for real and imaginary parts of \hat{q} decouple entirely across this region.

We solve the boundary value problem (6.5a) using a shooting method based on the `ode15s` solver implemented in MATLAB; simulations are initiated from $x = x_0$, using the two specified boundary conditions (6.5c). In addition, we adjust the values of the boundary conditions $\hat{q}_{1,xx}(x_0^-)$ and $\hat{q}_{1,xxx}(x_0^-)$ to isolate solutions which obey the appropriate boundary conditions at $x = 0$ (6.5b). However, the boundary value problem (6.5a) is locally singular at $x = x_0$ since $\hat{h}_1^{(s)}(x_0) = 0$. To initiate a numerical simulation we shoot from a small distance δ upstream of x_0 ($\delta \ll 1$) toward the upstream boundary ($x = 0$). We approximate the value of \hat{q}_1 and its derivatives at this point using a Taylor series expansion about x_0 . In simulations we found that a six term Taylor series with $\delta = 10^{-3}$ was sufficient to ensure convergence.

The corresponding perturbation membrane profile across region 1 is given by $\hat{h}_1 = -\hat{q}_{1,x}/\hat{\sigma}$. At neutral stability, assuming \hat{q}_1 is purely real implies that \hat{h}_1 will be purely imaginary.

6.2. Region 2

In a similar manner to region 1, across region 2 ($x_0 \leq x \leq 1$, denoted with the subscript 2), we expand the static membrane profile according to

$$\hat{h}^{(s)} = \hat{h}_2^{(s)} + O(p_e^{-1/2}). \quad (6.6)$$

In region 2 the leading-order static governing equations (2.9) become

$$\hat{h}_{2,xxx}^{(s)} = 0, \quad (x_0 \leq x \leq 1), \quad (6.7a)$$

subject to boundary conditions

$$\hat{h}_2^{(s)}(x_0) = 0, \quad \hat{h}_2^{(s)}(1) = 1, \quad \hat{h}_{2,xx}^{(s)}(1) = \hat{T}^{-1}. \quad (6.7b)$$

This system can be easily solved to obtain

$$\hat{h}_2^{(s)}(x) = \frac{1}{2}\hat{T}^{-1}(x-1)(x-x_0) + \frac{(x-x_0)}{(1-x_0)}, \quad (x_0 \leq x \leq 1). \quad (6.7c)$$

To construct an approximation to the perturbation eigenfunction across region 2 we expand the dependent variables according to

$$\tilde{h} = p_e^{-1/2}\hat{h}_2 + O(p_e^{-1}), \quad (6.8a)$$

$$\tilde{q} = \hat{q}_2 + O(p_e^{-1/2}). \quad (6.8b)$$

The perturbation governing equations (2.11) in region 2 take the leading-order form

$$\hat{\sigma}^2 \hat{q}_2 + \hat{T} \hat{h}_2^{(s)} \hat{q}_{2,xxxx} = 0, \quad (x_0 \leq x \leq 1), \quad (6.9a)$$

subject to

$$\hat{q}_2 = 0, \quad \hat{q}_{2,x} = 0, \quad (x = x_0), \quad (6.9b)$$

$$\hat{q}_2 = 0, \quad \hat{T} \hat{q}_{2,xxx} = L_2 \hat{\sigma}^2 \hat{q}_2, \quad (x = 1). \quad (6.9c)$$

This represents a similar balance of terms to region 1.

Again this problem is locally singular at $x = x_0$ and we employ an analogous numerical method to that described in §6.1 to construct a solution; we shoot from a small distance

δ downstream of the constriction x_0 using the boundary conditions (6.9b) toward the downstream boundary at $x = 1$, adjusting the value of $\hat{q}_{2,xx}(x_0^+)$ and $\hat{q}_{2,xxx}(x_0^+)$ to identify solutions which satisfy the boundary conditions (6.9c).

The corresponding perturbation membrane profile across region 2 is then given by $\hat{h}_2 = -\hat{q}_{2,x}/\hat{\sigma}$. As before, at neutral stability we assume \hat{q}_2 is purely real, so \hat{h}_2 must be purely imaginary.

6.3. Region 3

In region 3, close to the point of maximal constriction at $x = x_0$, we rescale the variables according to

$$x = x_0 + p_e^{-1}X, \quad h^{(s)}(x) = p_e^{-1}\hat{H}_3^{(s)}(X) + O(p_e^{-3/2}). \quad (6.10)$$

Hence, across region 3, the leading-order governing equation for the static membrane shape (2.9) becomes

$$\frac{6}{5} \left(\frac{1}{\hat{H}_3^{(s)}} \right)_X = \hat{T}\hat{H}_3^{(s)}\hat{H}_{3,XXX}^{(s)}, \quad (6.11a)$$

representing an inviscid balance between convective inertia and the restoring force of membrane tension. This equation is subject to continuity of slope in the far field with regions 1 and 2, in the form

$$\hat{H}_{3,X}^{(s)} \rightarrow \frac{1}{2}\bar{A}_1x_0 - \frac{1}{x_0}, \quad \text{as } X \rightarrow -\infty, \quad (6.11b)$$

$$\hat{H}_{3,X}^{(s)} \rightarrow \frac{1}{2}\hat{T}^{-1}(x_0 - 1) + \frac{1}{(1 - x_0)}, \quad \text{as } X \rightarrow \infty. \quad (6.11c)$$

Following Xu & Jensen (2015), we integrate (6.11a) twice to form an explicit expression for the membrane slope in the form

$$\hat{T} \left(\hat{H}_{3,X}^{(s)} \right)^2 = \frac{6}{5} \left(\frac{1}{H_0} - \frac{1}{\hat{H}_3^{(s)}} \right), \quad (6.12)$$

where $\hat{H}_3^{(s)}(0) = H_0$ is an unknown parameter. Following Xu & Jensen (2015), we can integrate once more to obtain an implicit expression for the membrane shape across region 3,

$$\sqrt{\frac{6}{5\hat{T}H_0^3}}X = \frac{1}{H_0} \sqrt{\hat{H}_3^{(s)}(\hat{H}_3^{(s)} - H_0)} + \log \left[H_0^{-1/2} \left(\sqrt{\hat{H}_3^{(s)}} + \sqrt{(\hat{H}_3^{(s)} - H_0)} \right) \right]. \quad (6.13)$$

For use below, following Xu & Jensen (2015) it can also be shown that

$$\int_{-\infty}^{\infty} \frac{1}{(\hat{H}_3^{(s)})^3} dX = \frac{8}{3} \sqrt{\frac{5\hat{T}}{6H_0^3}}. \quad (6.14)$$

Furthermore, to construct an approximation to the perturbation eigenfunction across region 3 we expand the dependent variables according to

$$\tilde{h} = p_e^{-3/2}\hat{H}_3(X) + O(p_e^{-2}), \quad (6.15a)$$

$$\tilde{q} = p_e^{-1/2}\hat{Q}_3(X) + O(p_e^{-1}). \quad (6.15b)$$

(m, n)	x_0	$\hat{\beta}$	\hat{R}_c	H_0	$\hat{q}_{1,xxx}(x_0^-)$	$\hat{q}_{2,xxx}(x_0^+)$
(2,1)	0.8602	16.9155	77.2746	0.1296	5.9757	14.4295
(2,2)	0.4965	21.0966	-9.3319	11.3413	12.1251	12.1850
(2,3)	0.3832	27.6437	-0.0002697	955.1028	19.4665	25.6459
(3,1)	0.9356	54.5129	453.0300	0.02543	9.7457	31.1619
(3,2)	0.6339	45.0394	4.6292	1.8186	16.7458	15.8465
(3,3)	0.4988	54.7264	-28.5297	10.8957	24.1992	24.2137
(4,1)	0.9632	126.9541	1497.483	0.008164	13.9429	54.5218
(4,2)	0.7195	80.1472	11.469	0.7319	21.3098	20.3208
(4,3)	0.5905	90.3640	3.1162	2.9839	28.5925	28.0238

TABLE 1. Shooting parameters for the nine eigenmodes shown on figure 8 computed for $\hat{T} = 0.2$ and $L_2 = 3$.

The leading-order perturbation equations across region 3 become

$$\hat{Q}_{3,X} = 0, \quad \hat{T} \hat{H}_{3,XXX} = \frac{6}{5} \left(-\frac{2\hat{Q}_3 H_{3,X}^{(s)}}{(H_3^{(s)})^3} - \frac{\hat{H}_{3,X}}{(H_3^{(s)})^3} + \frac{3\hat{H}_3 \hat{H}_{3,X}^{(s)}}{(H_3^{(s)})^4} \right), \quad (6.16)$$

subject to appropriate matching conditions into regions 1 and 2. However, noting that these equations are symmetric in X we find below that we do not need to solve the perturbation equations in this region explicitly to construct the outer approximation to the eigenfunctions.

6.4. The composite static solution

Matching the expression for $\hat{H}_{3,X}^{(s)}$ as $X \rightarrow -\infty$ into region 1 we obtain the constant \bar{A}_1 in the form

$$\bar{A}_1 = \hat{T}^{-1} \frac{1-x_0}{x_0} - \frac{2(2x_0-1)}{x_0^2(1-x_0)}, \quad (6.17)$$

while matching the expression for $\hat{H}_{3,X}^{(s)}$ as $X \rightarrow \infty$ into region 2 we obtain a constraint for H_0 as a function of x_0 ,

$$\frac{6}{5} \left(\frac{1}{H_0} \right) = \frac{1}{2} \frac{(x_0-1)}{\hat{T}} + \frac{1}{1-x_0}. \quad (6.18)$$

This fully specifies the leading-order static solution across all three regions for a given x_0 . Using the value of x_0 calculated in §6.5 and the critical value of Reynolds number \hat{R} calculated in §6.6, we thus plot the approximation to the membrane shape across the three regions in figure 7 for three examples (figure 7(b,i), (c,i) and (d,i)), showing excellent qualitative agreement with full numerical simulations in the first two cases; a discussion of the discrepancy for mode (2,1) is given in §6.7.

6.5. The oscillation frequency and point of maximal constriction

Since we are only concerned with neutrally stable oscillations, we express $\hat{\sigma}^2 = -\hat{\beta}^2$ and conduct all calculations in terms of $\hat{\beta}$. Given that $\hat{\beta}^2$ is purely real at neutral stability, the form of the governing equations (6.5a,6.9a) mean that the real and imaginary parts of \hat{q} can be considered independently at this order.

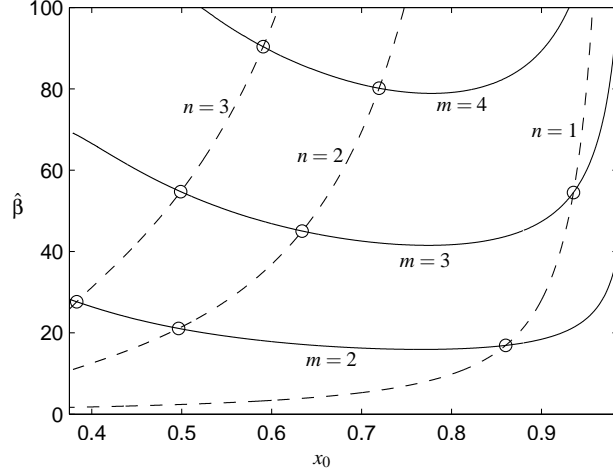


FIGURE 8. Parameter space spanned by the position of the membrane minimum x_0 against the corresponding oscillation frequency $\hat{\beta}$ for $\hat{T} = 0.2$ and $L_2 = 3$. Solid (dashed) lines represent solutions which satisfy the upstream (downstream) boundary conditions. Crossing points represent global roots of the asymptotic system.

Across region 3 we observe that the membrane profile is symmetric to leading-order, so that the limiting slopes from regions 1 and 2 are equal and opposite,

$$\lim_{x \rightarrow x_0^+} \hat{h}_{2,x} = - \lim_{x \rightarrow x_0^-} \hat{h}_{1,x}. \quad (6.19)$$

Since the solution to the linearised system (2.11) can be normalised arbitrarily, we set $\hat{q}_{xx}(x_0^+) = 1 = -\hat{q}_{xx}(x_0^-)$ without loss of generality (since \hat{q}_{xx} is proportional to \hat{h}_x through (2.11a)). For a given value of x_0 we compute the corresponding values of $\hat{\beta}$ and $\hat{q}_{xx}(x_0^-)$ ($\hat{q}_{xx}(x_0^+)$) such that the solution satisfies the upstream (downstream) boundary conditions, from which we trace out curves in the parameter space spanned by x_0 and $\hat{\beta}$; each curve represents a different number of extrema in the profile of h denoting m (n) turning points upstream (downstream) of the point of maximal constriction. In figure 8, typical curves for $m = 2$, $m = 3$ and $m = 4$ are shown as solid lines while curves for $n = 1$, $n = 2$ and $n = 3$ are shown as dashed lines, computed for $\hat{T} = 0.2$ and $L_2 = 3$. Numerical tests indicate there is no curve for $m = 1$. Points of intersection between upstream (solid) and downstream (dashed) curves in figure 8 represent global roots of the full system. These global crossing points correspond to distinct modes with a particular (m, n) ; the critical values of x_0 and $\hat{\beta}$ for the first nine modes are listed in table 1, along with the corresponding shooting parameters.

The asymptotic prediction of the critical frequencies for modes (3,2), (4,2) and (2,1) are plotted against the full numerical solutions as filled circles in figures 4(c) and 10(b). We find excellent agreement with the computed frequencies, with the mode (2,1) corresponding to neutral curve (iib), the mode (3,2) corresponding to neutral curve (iv) and the mode (4,2) corresponding to the neutral curve (v). In addition, the corresponding asymptotic prediction of the maximal constriction ($p_e^{-1}H_0$) and the point of greatest constriction (x_0) are shown in figures 10(c) and 10(d), respectively, against the full numerical computations. In both cases the curves (3,2) and (4,2) show excellent agreement with the numerical computations for neutral curves (iv) and (v). The curve (2,1) shows the correct trend as neutral curve (iib), but is slightly separated. The origin of this discrepancy is explored in §6.7 below.

6.6. *The critical Reynolds number*

Applying the scalings for regions 1 to 3 into the energy budget for static solutions (2.17), we obtain the leading-order relationship

$$\hat{T} \left(\hat{h}_{2,xx}^{(s)}(1) - \hat{h}_{1,xx}^{(s)}(0) \right) = \frac{12}{\hat{R}} \int_{-\infty}^{\infty} \frac{1}{(\hat{H}_3^{(s)})^3} dX, \quad (6.20)$$

so the rate of working of pressure forces along the compliant segment of the channel is balanced by the viscous losses close to the point of greatest channel constriction. Substituting the analytical expressions for $h_1^{(s)}$, $h_2^{(s)}$ constructed above (equations (6.3c) and (6.7c)) and the integral (6.14), we obtain the constraint

$$\frac{1}{\hat{T}x_0} + \frac{2(2x_0 - 1)}{x_0^2(1 - x_0)} = \frac{32}{\hat{R}} \left(\frac{5\hat{T}}{6H_0^3} \right)^{1/2}. \quad (6.21)$$

For a given x_0 and $\hat{\beta}$ computed using the method outlined above, the corresponding critical Reynolds number can be computed using (6.21). These predictions are listed in Table 1 and the corresponding predictions of the neutral curves are shown in figures 4(a) and 10(a) for modes (2,1), (3,2) and (4,2). As $p_e \rightarrow \infty$ the neutral curves each show the correct trend and approach the numerically computed curves, although the values of p_e considered here are not sufficiently large to demonstrate a strong overlap (as discussed above, we found that an unfeasible number of grid points were needed to resolve the static profile for larger values of p_e). There is a more marked discrepancy for the mode labelled (2,1), which is discussed below. For some of the roots identified in Table 1 the corresponding critical Reynolds number is negative, indicating an unphysical solution for those (m, n) and that choice of parameters \hat{T} and L_2 .

6.7. *Outer approximation to the eigenfunctions*

Given the approximate eigenfunction profiles constructed across regions 1 and 2 in §6.5, the outer asymptotic eigenfunctions for three particular examples are shown in figure 7(b,c,d) for $\hat{T} = 0.2$ and $L_2 = 3$. Note that the outer asymptotic eigenfunction has been normalised in the same way as the numerically computed eigenfunctions for ease of comparison. In particular, we consider mode (3,2) in figure 7(b,ii), (b,iii), where $R_c \approx 338.44$ ($p_e \hat{R}_c \approx 216.30$), mode (4,2) in figure 7(c,ii), (c,iii), where $R_c \approx 677.65$ ($p_e \hat{R}_c \approx 532.15$) and mode (2,1) in figure 7(d,ii), (d,iii), where $R_c \approx 320.09$ ($p_e \hat{R}_c \approx 605.69$). For modes (3,2) and (4,2) we observe excellent qualitative agreement between the numerically computed eigenfunctions and the outer asymptotic approximation. However, for mode (2,1) the agreement is weaker, exacerbated by the large discrepancy in the estimate of the point of maximal constriction (figure 10d). A possible explanation for this discrepancy lies in the shape of the eigenfunction downstream of the constriction. In this region, unlike for the other examples shown, the real and imaginary parts of \tilde{q} are comparable (figure 10(d,ii)), so our assumption that \tilde{q} is purely real is not appropriate. Furthermore, the slopes of the perturbation membrane shape upstream and downstream of the constriction are clearly not equal and opposite (figure 10(d,iii)), in contradiction of our leading-order asymptotic theory. To improve the prediction of this mode would require coupling of the real and imaginary parts of the eigenfunction at leading-order, which is not considered here.

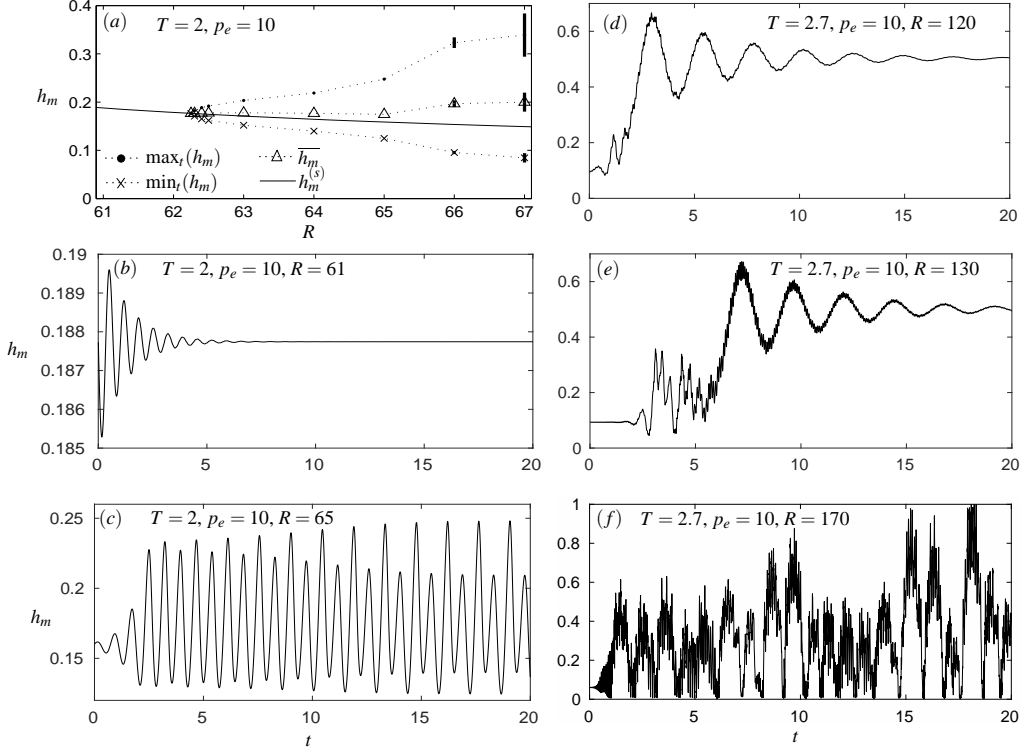


FIGURE 9. Fully nonlinear simulations for $p_e = 10$ and $L_2 = 3$: (a) bifurcation diagram of h_m against R for $T = 2$, tracing the maximum (filled circles) and minimum (crosses) of $h_m(t)$ over a period of oscillation; time-traces of the membrane minimum h_m for (b) $T = 2$, $R = 61$, where the response is asymptotically stable; (c) $T = 2$, $R = 65$, where the oscillatory response has undergone a period doubling bifurcation; (d) $T = 2.7$, $R = 120$ where the oscillation again saturates the almost uniform static state; (e) $T = 2.7$, $R = 130$ where the oscillation saturates to a large amplitude limit cycle with ‘slamming’. The triangles in (a) illustrate the mean position of the membrane minimum over a period, while the thick black lines indicate the range of values for the maximum and minimum of h_m for the chaotic oscillations.

7. Fully nonlinear simulations

In this section we use fully nonlinear simulations of the PDEs (2.8) to examine the nonlinear development of the primary global instability (§7.1), the corresponding nonlinear energy budget of fully developed oscillations (§7.3) and finally the development of nonlinear ‘slamming’ oscillations for large Reynolds numbers (§7.2).

7.1. Primary global instability

In figure 9(a) we show a close up of the neutral stability curve for $p_e = 10$ (figure 4a) around the region where the neutral curves for the most unstable modes terminate, close to $T \approx 2.100$. We use nonlinear simulations of (2.8) to trace the behaviour along two lines in parameter space with $p_e = 10$ and $L_2 = 3$, the first for $T = 2$ where the collapsed basic state exists for all R (§7.1) and the second for $T = 2.7$ where the collapsed basic state (§7.2) does not exist for sufficiently small R .

We examine the primary global instability close to the neutral point for $T = 2$, $p_e = 10$ for $L_2 = 3$, where the collapsed basic state becomes unstable to an oscillatory instability (via a Hopf bifurcation) as the Reynolds number increases through the threshold $R =$

$R_c \approx 62.24$. In simulations we employ an initial condition

$$h(x, 0) = h^{(s)}(x) + A\Re(\tilde{h}(x; \sigma)), \quad q(x, 0) = 1 + A\Re(\tilde{q}(x; \sigma)), \quad (7.1)$$

where $A = 0.01$ in simulations. In figure 9(a) we numerically trace a bifurcation diagram by plotting the minimal and maximal values of h_m over a period of fully developed oscillation as a function of R . Figure 9(a) indicates that the Hopf bifurcation is supercritical. For $R < R_c$ the static membrane is asymptotically stable (figure 9b). However, as the Reynolds number increases the oscillation undergoes a period doubling bifurcation (evident for $R = 65$, see figure 9c) and eventually becomes chaotic (evident for $R = 66$, $R = 67$, where the thick black lines indicate the range of values for the maximum and minimum of h_m). Also shown on figure 9(a) is the mean position of the membrane minimum over a period of oscillation, denoted $\overline{h_m}$ (illustrated as open triangles connected by a dotted line) compared to the minimal value of the corresponding static membrane (solid line). We observe that the mean minimal channel width is increased slightly compared to the static solution, which has consequences for the energy transfer mechanism sustaining the oscillation (see §7.3 below).

7.2. Fully nonlinear ‘slamming’ oscillations

We examine the secondary global instabilities by considering the fully nonlinear behaviour close to a region where the collapsed basic state does not exist, in particular for $T = 2.7$, $p_e = 10$ for $L_2 = 3$. For $R > R_b \approx 127.8$ we use the initial condition (7.1). For lower Reynolds numbers ($R < R_b$) the highly collapsed steady state does not exist. Starting close to the almost uniform static state the system is asymptotically stable (not shown). Hence, we choose to start the simulations close to the highly collapsed static state computed for some $R > R_b$ (here we choose an initial state generated for $R = 130$). For $R = 120$ the system oscillates initially but eventually saturates toward the almost uniform static state, as in figure 9(d). For $R > R_b$ the perturbation growth becomes increasingly oscillatory and irregular as R increases, where there are two possible attractors for long times. For some parameter choices inside the dark shaded region in figure 4(b) (where there are two concurrent static states) the system oscillates initially but eventually saturates to the almost uniform static profile, as shown in figure 9e for $R = 130$; for other parameter choices the system exhibits a fully developed oscillatory (typically chaotic) limit cycle, where periodically the membrane is drawn very close to the rigid wall before recovering (see example for $R = 170$ in figure 9f). These so-called ‘slamming’ oscillations have been observed previously (Stewart *et al.* 2010; Stewart 2010; Xu *et al.* 2013) and can be deconstructed using matched asymptotic expansions (Xu & Jensen 2015). As the Reynolds number increases the ‘slamming’ oscillation eventually becomes dominant. It is interesting to note that in this case linear instability to oscillations does not necessarily result in an unsteady outcome for long times, similar to predictions of three-dimensional flow in a collapsible tube by Heil & Boyle (2010).

7.3. Energy budget of the primary global instability

Finally, we examine the energy budget of the self-excited oscillations to elucidate the driving mechanism. We define the time average of a quantity $f(x, t)$ over a period of oscillation T_f according to

$$\overline{f}(x) = \frac{1}{T_f} \int_0^{T_f} f(x, t) dt. \quad (7.2)$$

In particular we consider a parameter sweep along the line $T = 2$ for $p_e = 10$, $L_2 = 3$ where the critical Reynolds number $R_c \approx 62.24$ corresponds to the mode labelled (i) in

T	R	p_e	$\mathcal{P}^{(s)}$	$\mathcal{D}^{(s)}$	$h_m^{(s)}$	$\overline{\mathcal{F}}$	$\overline{\mathcal{P}}$	$\overline{\mathcal{D}}_S$	$\overline{\mathcal{D}}_A$	\overline{h}_m
2.0	62.5	10.0	9.9994	9.9994	0.1746	-0.002118	9.8641	9.8640	-0.0020458	0.17664
2.0	63.0	10.0	10.302	10.302	0.1709	-0.006279	9.9205	9.9201	-0.0060039	0.17664
2.0	64.0	10.0	10.864	10.864	0.1644	-0.01489	10.037	10.036	-0.013990	0.17664
2.0	65.0	10.0	11.377	11.377	0.1587	-0.02375	10.220	10.214	-0.022658	0.17638

TABLE 2. Numerical values of time-averaged quantities in the fully nonlinear energy equation (2.13) and corresponding static energy equation (2.14) for simulations with fixed $T = 2$, $p_e = 10$ and $L_2 = 3$.

figure 4. The terms in the full energy budget (2.13a) are computed for various $R > R_c$ from the nonlinear simulations and their time-average calculated over a period of fully saturated oscillation and listed in Table 2. Also listed in the table are the terms in the energy budget for the corresponding static state, denoted with the superscript (s).

We compute the energy budget of the oscillation by subtracting the energy corresponding to the static state, computing the excess work done by upstream pressure forces over a period ($\overline{\mathcal{P}^{(e)}} = \overline{\mathcal{P}} - \mathcal{P}^{(s)}$) and the excess rate of working of viscous dissipation ($\overline{\mathcal{D}^{(e)}} = \overline{\mathcal{D}}_S - \mathcal{D}^{(s)}$). It emerges that over a period the dominant energy balance is between these excess energies, $\overline{\mathcal{P}^{(e)}}$ and $\overline{\mathcal{D}^{(e)}}$, while the net kinetic energy flux extracted from the mean flow ($\overline{\mathcal{F}}$) and the kinetic energy flux induced by the flow profile assumption ($\overline{\mathcal{D}}_A$) are both very small in comparison (see Table 2). This is in direct agreement with the observations of Liu *et al.* (2012) in a flow-driven collapsible channel system.

As discussed in §2.4, we further decompose $\overline{\mathcal{D}}_S$ using the global linear stability eigen-solver, where (2.19) implies

$$\overline{\mathcal{D}^{(e)}} \approx \theta^2(\overline{\mathcal{D}}_S + \overline{\mathcal{D}}_S), \quad (7.3)$$

for $\theta \ll 1$. In the fully nonlinear computations we find $\overline{\mathcal{D}^{(e)}} < 0$ for all cases tested (see Table 2). However, computing $\overline{\mathcal{D}}_S$ for these parameter values at criticality ($T = 2$, $p_e = 10$, $L_2 = 3$, $R_c \approx 62.24$) using the perturbation eigenfunctions \tilde{h} and \tilde{q} we find that $\widehat{\mathcal{D}}_S > 0$. Hence, dissipative forces in the perturbation are consuming energy, so the perturbation dissipation in the mean flow, $\overline{\mathcal{D}}_S$, must be negative. Hence, the presence of the oscillation reduces the overall dissipation of the mean flow (through the work of nonlinear Reynolds stresses) and this excess energy drives the oscillation. However, this reduction of the dissipation is not achieved by modifying the mean flow along the channel as we need $\overline{q}(1, t) = 1$ (*ie.* $\overline{q} = 0$) to satisfy conservation of mass over a period of neutrally stable oscillation. Instead this reduction in dissipation is achieved by decreasing the mean maximal constriction of the channel over a period of neutrally stable oscillation, so $\overline{h}_m > h_m^{(s)}$. This is illustrated in the fully nonlinear bifurcation diagram in figure 9(a) and the computed values of \overline{h}_m and $h_m^{(s)}$ are listed in Table 2.

A similar mechanism of energy transfer is operating for the mode labelled (ia), corresponding to the most unstable member of the family of high-frequency oscillations explored in §6.

8. Discussion

In this paper we have considered the stability of laminar high-Reynolds-number flow through a planar channel, where a section of one wall has been replaced by a tensioned membrane; this tension is assumed sufficiently large to dominate the influence of bending stiffness and other elastic restoring forces. The model also neglects other wall parameters such as the wall inertia and viscous damping, although the role of these parameters will be considered in future work. To reduce the computational complexity, we construct a spatially one-dimensional model derived using a von-Karman–Pohlhausen approximation in a similar manner to earlier studies of flow through a flexible-walled channel (Stewart *et al.* 2009; Xu *et al.* 2013, 2014; Xu & Jensen 2015). This model has a number of limitations, most notably its failure to capture the influence of dissipation in narrow boundary layers that will arise at large Reynolds numbers and frequencies. In addition, this model fails to capture energy losses associated with flow separation (discussed below) and the generation of so-called vorticity waves in the downstream rigid segment (a striking feature of computational simulations driven by fixed upstream flux, Luo & Pedley (1996)). However, this model has previously been demonstrated to give good qualitative agreement with full numerical simulations at modest Reynolds numbers, successfully predicting several families of self-excited oscillations also found in the full two-dimensional system including ‘sloshing’ oscillations (Jensen & Heil 2003; Stewart *et al.* 2009), ‘sawtooth’ oscillations (Xu *et al.* 2014) and nonlinear ‘slamming’ oscillations (Stewart *et al.* 2010). The model also provides a method for examining large sections of the parameter space with relatively low computational cost.

Energy losses associated with flow separation were a key feature of earlier one-dimensional models of oscillations in collapsible tubes (eg Cancelli & Pedley 1985; Jensen 1990), necessary for the system to exhibit instability in the absence of other sources of dissipation. In the present model, the additional energy losses due to flow separation might be expected to increase the critical Reynolds number required for instability of our global modes. This hypothesis is corroborated by preliminary simulations of our linear stability eigensolver where the convective inertia term in (2.8b) is multiplied by a constant $\chi < 1$ in the region downstream of maximal constriction, in a similar manner to previous one-dimensional models (eg Cancelli & Pedley 1985; Jensen 1990). However, such a crude modification fails to accurately account for the recirculation region in the flow downstream of the point of separation (see Luo & Pedley 2000) and its influence on the dissipative losses, neither of which can be rationally captured within our flow profile assumption. A more complete examination of the influence of flow separation on our predicted modes of oscillation is therefore deferred to future work.

In particular, we consider a constant external pressure applied to the flexible membrane, in contrast to previous studies using this one-dimensional model which all imposed an external pressure gradient which is difficult to realise experimentally. The flow is driven by a fixed upstream flux, and we demonstrate that the system admits at least one non-uniform static state at all points across the parameter space. For sufficiently large Reynolds numbers, across a range of membrane tensions the system exhibits three possible static solutions, two of which are stable to (static) perturbations (figure 2). This prediction of multiple co-existing steady states is consistent with previous one-dimensional models of collapsible tube flow (Reyn 1987; Siviglia & Toffolon 2014) and full numerical computations of flow through flexible-walled channels (Luo & Pedley 2000) and tubes (Heil & Boyle 2010).

The static predictions of figure 2(a) can be represented in an alternative manner, plotting the flow rate along the channel as a function of the applied driving pressure, while

holding the difference between the upstream and external pressures constant. Similar to previous studies (eg Jensen 1998; Luo & Pedley 2000; Stewart 2010), the flow rate eventually becomes limited by the constriction and does not continue to increase with increasing driving pressure. Such ‘flow limitation’ or ‘choking’ can occur physiologically when forced expiration from the lungs causes airways to collapse, restricting the flow of air (Gavriely & Grotberg 1988). In previous one-dimensional models, such choking behaviour was associated with a transition through the critical state (Kececioglu *et al.* 1981; Cancelli & Pedley 1985; Elad *et al.* 1987) *ie* the flow speed approaching the local wave speed. A more recent study by Siviglia & Toffolon (2013) showed how these transcritical conditions could be induced by discontinuous mechanical properties of the flexible vessel, physiologically mimicking a stent or region of tissue whose properties have been altered by surgery. However, given the dispersive nature of the current model it is not clear if a similar transition occurs in our predictions.

For low Reynolds numbers the system is asymptotically stable. However, as the Reynolds number increases (holding other parameters fixed) the static configuration becomes unstable to self-excited oscillations via a supercritical Hopf bifurcation. The non-uniform state is unstable to two infinite families of oscillatory normal modes, all with distinct neutral curves. Some of these neutral curves trace out two branch tongues beyond a critical membrane tension, similar to those found by Luo *et al.* (2008), while others persist for all tensions (figures 4, 10). Testing of these new predictions against full two-dimensional computations is an interesting avenue of future work.

For sufficiently low membrane tensions, the primary global instability of the system is to a low-frequency mode where the frequency of oscillation decreases as p_e increases; the corresponding eigenfunction for the perturbation membrane shape has two extrema for low tensions (mode-2) (figure 7(a,iii)) but changes form along the neutral curve as the tension increases (figure 3b). As $p_e \rightarrow \infty$ the mode-2 static membrane shape arises from an outwardly bulged region in the centre of the domain with a narrow constriction at the downstream end (figure 7(a,i)). The corresponding neutral stability curves continue as $T \rightarrow 0$, and the corresponding critical Reynolds number at onset takes the simple form $R_c = 12L_2/p_e$ as $p_e \rightarrow \infty$ (figure 6a). It is interesting to note that the parameter regime where this instability is predicted (low Reynolds number, low-frequency oscillations) is exactly that where the present one-dimensional model is expected to be an accurate reflection of the full two-dimensional system.

For larger membrane tensions, we identified an alternative asymptotic regime where the frequency of oscillation increases with increasing external pressure (figure 4c). Most of these high-frequency modes exhibit a two branch neutral curve, unstable beyond a critical value of the tension (figure 4a). For modes along the lower branch of these neutral curves, either side of the point of maximal constriction there is a leading-order balance between the unsteady inertia and the restoring force of membrane tension. This leading-order balance (along with the observation that the oscillation frequency increases with the square root of the membrane tension), is identical to that observed for ‘sloshing’ instabilities driven by fixed upstream pressure (Jensen & Heil 2003; Stewart *et al.* 2009). However, in the present case the dominant source of viscous dissipation arises around the point of greatest constriction of the static membrane, whereas for ‘sloshing’ modes predicted in using an analogue of our 1D model the dominant dissipation arises over entire channel (Stewart *et al.* 2009). (Of course, in the full 2D and 3D representations of ‘sloshing’ the dominant dissipation is confined to narrow Stokes layers on the channel walls (Jensen & Heil 2003; Whittaker *et al.* 2010).) In addition, in ‘sloshing’ the mean flow rate along the channel is increased by the oscillation, whereas here the mean flow must remain constant (due to the choice of upstream boundary condition) and instead the

channel walls are driven apart over a period, releasing energy which drives the oscillation. Hence, although the leading-order balance of terms is broadly similar, the fundamental mechanism of instability elucidated herein is very different to ‘sloshing’. The asymptotic structure divides the perturbation membrane profile into two distinct segments and leads to a new naming convention: mode (m, n) has m extrema upstream of the point of greatest constriction and n extrema downstream. Predictions of modes (3,2) and (4,2) (and to a lesser extent mode (2,1)) all agree well with the corresponding numerical computations (figures 4,10) as p_e becomes large.

In regions of the parameter space where the system exhibits two stable static states (eg. shaded region in figure 4b), nonlinear simulations of the governing equations about the highly collapsed static state exhibit one of two possible behaviors, depending on the choice of initial perturbation: in some cases the unsteady oscillation is eventually suppressed and the system asymptotes toward the almost uniform static state (figure 9d), while in others the system enters a large amplitude chaotic ‘slamming’ limit cycle (figure 9e), as have been observed previously in a similar system driven by fixed upstream flux (Xu *et al.* 2013, 2014; Xu & Jensen 2015). This chaotic response is consistent with the presence of homoclinic (global) bifurcation points nearby in the parameter space, which result from the intersection between the oscillatory neutral curves (associated with a supercritical Hopf bifurcation) and the line of limit points associated with loss of existence of the highly collapsed static state (figure 5).

The system considered herein, flow-driven oscillations about a highly collapsed static configuration is reminiscent of instabilities generated by fluid-structure interaction in the vocal folds in the human larynx (see Mittal *et al.* 2013, for a recent review), with the external pressure playing the role of the tissue pressure in the folds. A qualitative comparison between our predictions and experiments on mechanical replica of the human vocal tract is an interesting direction for future work. The model presented herein also has potential bio-mechanical application to snoring and sleep apnea (eg. Gavriely & Jensen 1993).

Acknowledgements

Helpful discussions with Prof. Oliver Jensen (University of Manchester), Prof. Xiaoyu Luo and Miss Danyang Wang (both University of Glasgow) are very gratefully acknowledged. Funding from EPSRC grant no. EP/N014642/1 is gratefully acknowledged. The data for the simulations presented in this paper can be accessed online (<http://dx.doi.org/10.5525/gla.researchdata.412>).

Appendix A. Inviscid static solutions for fixed upstream flux

Xu *et al.* (2013) found that their system (almost identical to (2.9) but with an imposed external pressure gradient to maintain a uniform basic state) admitted a countably infinite number of static, inviscid eigenmodes for particular values of the dimensionless membrane tension,

$$T_n = \frac{6}{5n^2\pi^2}, \quad n = 0, 1, 2, \dots \quad (\text{A } 1)$$

These critical values of the tension serve as organising centers for the dynamical system, as elucidated by Xu *et al.* (2013).

In a similar spirit, we examine the inviscid limit of the static governing equations (2.9)

for fixed external pressure, where the equations take the form

$$\frac{6}{5} \left(\frac{1}{h^{(s)}} \right)_x = Th^{(s)} h_{xxx}^{(s)}, \quad (0 \leq x \leq 1), \quad (\text{A } 2a)$$

subject to three boundary conditions

$$h^{(s)} = 1, \quad (x = 0), \quad (\text{A } 2b)$$

$$h^{(s)} = 1, \quad Th_{xx}^{(s)} = p_e, \quad (x = 1), \quad (\text{A } 2c)$$

independent of the downstream length of the channel, L_2 . These static inviscid governing equations (A 2) can be integrated exactly to obtain a second order ODE

$$\frac{3}{5} \left(\frac{1}{(h^{(s)})^2} - 1 \right) = Th_{xx}^{(s)} - p_e, \quad (0 \leq x \leq 1), \quad (\text{A } 3)$$

subject to $h^{(s)}(0) = h^{(s)}(1) = 1$. This equation can be integrated once more with respect to x , but it was not possible (to the best of our knowledge) to find a closed form solution for $h^{(s)}(x)$. However, (A 3) can be easily solved numerically and the properties of $h^{(s)}$ can be traced as a function of the model parameters. It emerges that for a given p_e there are two branches of inviscid static solutions for $T > T_c$, beyond a limit point at $T = T_c$, as shown in figure 2, a stable upper branch and an unstable lower branch. For $p_e = 10$, the critical value of T above which these static inviscid solutions exist is $T_c \approx 2.426$, much greater than the largest admissible value of membrane tension found by Xu *et al.* (2013) listed in (A 1), representing a significant difference between application of a fixed external pressure and an external pressure gradient.

Appendix B. Numerical results for \hat{T} constant

We further illustrate the parameter space of neutrally stable oscillations in an alternative manner, holding both the downstream channel length and ratio of membrane tension to external pressure fixed ($\hat{T} = T/p_e = \text{constant}$, where $\hat{T} = T_0/(\rho a(P_e - P_0))$ in terms of dimensional variables). This choice of scaling is consistent with the asymptotic structure identified in §6. For example, setting $\hat{T} = 0.2$ and $L_2 = 3$ the corresponding neutral curves for the six most unstable modes traced in figure 4, plotting the critical value of the Reynolds number as a function of the external pressure, are shown in figure 10(a), the corresponding oscillation frequency (figure 10b), the maximal constriction of the collapsed static channel ($h_m^{(s)}$, figure 10c) and the corresponding x -position of the that maximal constriction ($x_m^{(s)}$, figure 10d). The latter exhibits a step-wise structure as the membrane shape is solved on a uniform grid, so the location of the membrane minimum changes discretely. In this case the lower branch of the neutral curves become parallel in the limit as $p_e \rightarrow \infty$ and again terminate at a co-dimension 2 (global) bifurcation. As in figure 4, the neutral curves that do not terminate in an open circle continue to larger values of p_e than those considered here.

Appendix C. Low-frequency oscillations for $p_e \rightarrow \infty$

In this appendix we outline the asymptotic structure of the low-frequency instabilities in the limit $p_e \rightarrow \infty$, considering the leading-order static configuration and the corresponding leading-order perturbation eigenfunction. However, we do not calculate the critical conditions for the onset of instability, which follow from higher orders. We assume the flow can be decomposed into two asymptotic regions, a core region of $O(1)$

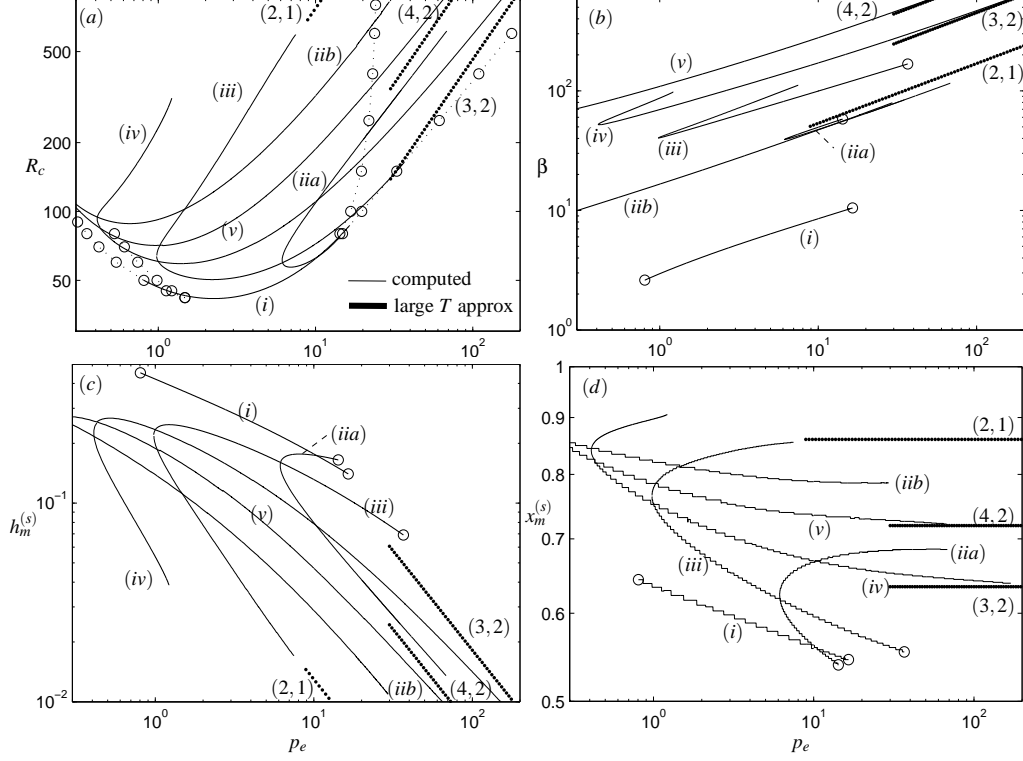


FIGURE 10. Neutrally stable oscillations for $\hat{T} = T/p_e = 0.2$ and $L_2 = 3$ as a function of the external pressure p_e : (a) the critical value of the Reynolds number of instability for the five most unstable modes labelled (i-v); (b) corresponding frequency of the neutrally stable modes; (c) minimal value of the constriction of the static state $h_m^{(s)}$; (d) the location of the minimal value of the static constriction, $x_m^{(s)}$. Also shown are the corresponding asymptotic predictions for large p_e for the three modes with lower branch that persists for $p_e \rightarrow \infty$.

width across the interior of the domain, where the static profile of the membrane is highly bulged outwards, denoted as region 1 (§C.1), and a narrow boundary layer at the downstream end of width $p_e^{-1/2} \ll 1$, denoted as region 2 (§C.2). We now consider each region in turn. In this appendix we denote the parameters and independent variables in the asymptotic problems with a breve to distinguish from their equivalents in the full problem, and a numbered subscript to denote the region where the variable is defined.

We assume that the critical Reynolds number can be expanded in powers of $p_e^{-1/2}$ in the form

$$R_c = p_e^{-1}(\breve{R}_c + p_e^{-1/2}\breve{R}_p + \dots), \quad (\text{C1})$$

where breved variables are $O(1)$. Furthermore, we rescale the membrane tension parameter in the form $T = p_e^{-1/2}\breve{T}$, where $\breve{T} = O(1)$, so this family of self-excited oscillations exists for low membrane tensions.

We consider neutrally stable oscillations and restrict attention to the case $\sigma = i\beta$ (the case $\sigma = -i\beta$ follows in an identical manner). We expand this critical frequency in the form,

$$\beta = p_e^{-1/2}\breve{\beta} + O(p_e^{-1}). \quad (\text{C2})$$

In the analysis below we will assume that at leading-order the perturbation eigenfunction

\tilde{h} is purely real and \tilde{q} is purely imaginary, consistent with the numerical examples in figure 7(a,ii), (a,iii).

C.1. Region 1

Across region 1 ($0 \leq x \leq 1$), the static membrane profile is significantly bulged and we rescale according to

$$h^{(s)} = p_e^{1/2} \check{h}_1^{(s)} + O(1). \quad (\text{C } 3)$$

In this case the leading-order governing equations for the static membrane shape (2.9) take the reduced form

$$\check{h}_{1,xxx}^{(s)} = 0, \quad (\text{C } 4a)$$

subject to outer boundary conditions

$$\check{h}_1^{(s)}(0) = \check{h}_1^{(s)}(1) = 0. \quad (\text{C } 4b)$$

The pressure boundary condition at the downstream end (2.9c) evaluated to leading-order gives no information about $\check{h}^{(s)}$ and instead determines a constraint for \check{R}_c in the simple form

$$\check{R}_c = 12L_2. \quad (\text{C } 5)$$

To satisfy the downstream boundary conditions at the following order we must introduce a narrow boundary layer (region 2), as discussed in §C.2 below.

The system (C 4) is easily integrated to give the parabolic form

$$\check{h}_1^{(s)}(x) = 4\check{h}_M^{(s)}x(1-x), \quad (\text{C } 6)$$

where $\check{h}_M^{(s)} = \max_x(\check{h}_1^{(s)})$ is the maximal membrane deflection, an unknown constant which is determined by matching into region 2.

To capture the structure of the perturbation across region 1, we expand the dependent variables according to

$$\tilde{h} = p_e^{1/2}\check{h}_1 + O(1), \quad \tilde{q} = \check{q}_1 + O(p_e^{-1/2}). \quad (\text{C } 7)$$

To leading-order the perturbation governing equations (2.11) across region 1 take the form

$$i\check{\beta}\check{h}_1 + \check{q}_{1,x} = 0, \quad \check{h}_{1,xxx} = 0, \quad (\text{C } 8a)$$

subject to boundary conditions at the upstream end

$$\check{h}_1 = 0, \quad \check{q}_1 = 0, \quad (x = 0). \quad (\text{C } 8b)$$

This system can be solved across $0 \leq x \leq 1$ in the form

$$\check{h}_1 = \frac{1}{2}\check{a}x^2 + \check{b}x, \quad (\text{C } 9a)$$

$$\check{q}_1 = -i\check{\beta}\left(\frac{1}{6}\check{a}x^3 + \frac{1}{2}\check{b}x^2\right), \quad (\text{C } 9b)$$

where \check{a} and \check{b} are real constants, determined by matching into region 2.

C.2. Region 2

Close to the downstream end of the channel at $x = 1$, we rescale in a narrow boundary layer according to

$$x = 1 - p_e^{-1/2}\xi, \quad (\text{C } 10)$$

where ξ is assumed $O(1)$. We expand the static membrane profile according to

$$h^{(s)}(x) = \check{H}_2^{(s)}(\xi) + O(p_e^{-1/2}), \quad (\text{C } 11)$$

where the leading-order governing equations for the static membrane shape (2.9) across region 2 take the form

$$(\check{H}_2^{(s)})^3 \check{H}_{2,\xi\xi\xi}^{(s)} = \frac{12L_2}{\check{T}\check{R}_c}. \quad (\text{C } 12a)$$

The pressure boundary condition at $\xi = 0$ (2.9c) at leading-order implies the constraint (C 5). The first order correction to the Reynolds number (denoted \check{R}_p) then appears in the boundary conditions expanded to next order, in the form

$$\check{T}\check{H}_{2,\xi\xi}^{(s)}(0) = \frac{12L_2}{\check{R}_c^2}\check{R}_p, \quad \check{H}_2^{(s)}(0) = 1. \quad (\text{C } 12b)$$

The ODE system (C 12) is solved numerically using a shooting method. For general initial conditions this ODE admits a solution which is quadratic in ξ as $\xi \rightarrow \infty$. Hence, to match to region 1 we numerically adjust the value of free parameter $\check{H}_{2,\xi}^{(s)}(0)$ to obtain a solution with constant slope in the far-field, (*ie.* $\check{H}_{2,\xi\xi}^{(s)} \rightarrow 0$ as $\xi \rightarrow \infty$). The corresponding value of the membrane slope as $\xi \rightarrow \infty$ is denoted $\check{H}_{M,\xi}^{(s)}$.

The perturbation variables across region 2 are expanded according to

$$\check{h} = \check{H}_2 + O(p_e^{-1/2}), \quad \check{q} = \check{Q}_2 + p_e^{-1/2}\check{\check{Q}}_2 + O(p_e^{-1}); \quad (\text{C } 13)$$

the leading-order perturbation governing equations (2.11) across region 2 take the form

$$\check{\check{Q}}_{2,\xi} = 0, \quad \check{T}\check{H}_2^{(s)}\check{H}_{2,\xi\xi\xi} = \check{H}_2 \left(\frac{24}{\check{R}_c(\check{H}_2^{(s)})^3} - \check{T}\check{H}_{2,\xi\xi\xi}^{(s)} \right), \quad (\text{C } 14a)$$

subject to boundary conditions at $\xi = 0$, which take the leading-order form

$$\check{\check{Q}}_2(0) = 0; \quad (\text{C } 14b)$$

these do not give any information about the shape of \check{H}_2 . We expand to the following order, where we obtain

$$\check{H}_2(0) = 0, \quad \check{T}\check{H}_{2,\xi\xi}(0) = -\frac{12L_2}{\check{R}_c}\check{\check{Q}}_2(0). \quad (\text{C } 14c)$$

For a given value of $\check{\check{Q}}_2(0)$, the ODE system (C 14) can be solved numerically for a suitably chosen value of $\check{H}_{2,\xi}(0)$. It should be noted that our assumption that \check{H}_2 is purely real requires that $\check{\check{Q}}_2(0)$ is also real, consistent with the perturbation eigenfunction \check{q} shown in figure 7(a,ii). As with the static problem across region 2, the generic behaviour of this ODE exhibits a solution which grows quadratically as $\xi \rightarrow \infty$. Hence, we must adjust the value of $\check{H}_{2,\xi}(0)$ to isolate the unique solution with constant slope in the far field ($\check{H}_{2,\xi\xi} \rightarrow 0$ as $\xi \rightarrow \infty$). The corresponding (constant) far field slope is denoted

$$\check{H}_{2,\xi} \rightarrow \check{H}_{M,\xi} \quad \text{as} \quad \xi \rightarrow \infty. \quad (\text{C } 15)$$

C.3. Matching between regions 1 and 2

Matching the static membrane slope between regions 1 and 2,

$$\lim_{x \rightarrow 1} \check{h}_{1,x}^{(s)} = - \lim_{\xi \rightarrow \infty} \check{H}_{2,\xi}^{(s)}, \quad (\text{C } 16)$$

we obtain the unknown constant in the solution across region 1 (C 6),

$$\check{h}_M^{(s)} = -\frac{1}{4}\check{H}_{M,\xi}^{(s)}. \quad (\text{C } 17)$$

To compute the perturbation eigenfunction, we match the perturbation flux and the perturbation membrane slope between regions 1 and 2. The leading-order perturbation flux across region 2 is zero, $\check{Q}_2(\xi) = 0$, and matching into region 1 tells us that $q_1(1) = 0$. Applying this condition determines the real constant \check{a} , where (C 9) becomes

$$\check{h}_1 = \frac{1}{6}\check{a}(3x^2 - 2x), \quad (\text{C } 18a)$$

$$\check{q}_1 = \frac{1}{6}i\check{\beta}\check{a}x^2(1-x). \quad (\text{C } 18b)$$

The remaining constant \check{a} is determined by matching the slope of the perturbation membrane shape between regions 1 and 2 in the form

$$\lim_{x \rightarrow 1} \check{h}_{1,x} = - \lim_{\xi \rightarrow \infty} \check{H}_{2,\xi}. \quad (\text{C } 19)$$

C.4. Static energy budget

Applying the rescalings for regions 1 and 2 into the static energy budget (2.14), we obtain at leading-order relationship,

$$\check{T}\check{H}_{\xi\xi}^{(s)} = \frac{12}{R_c} \int_0^\infty \frac{1}{(\check{H}^{(s)})^3} d\xi; \quad (\text{C } 20)$$

this is simply an integrated form of the static governing equation across region 2 (C 12), so no additional information is gleaned at this order.

C.5. Higher-order terms

It emerges that in this asymptotic expansion the influence of convective inertia emerges in the second-order correction across region 1 and the first-order correction across region 2. Similarly, the influence of unsteady inertia emerges in the second-order correction across region 1 and in the fourth-order correction across region 2. For finite p_e the numerically computed critical Reynolds number for instability is always greater than zero ($R_c > 0$), so the effect of inertia is necessary to trigger the onset of self-excited oscillations. It is possible to extend this analysis to higher orders to characterise the critical conditions for instability, including \check{R}_p and higher corrections to the Reynolds number, which are undetermined in the leading-order calculation. However, this is not pursued further here as the expansion results in a cumbersome set of governing equations in each region which must be solved numerically, with complicated matching required at each order.

C.6. Comparison to numerical simulations

We consider a particular example for $T = 0.01$, $p_e = 1000$ and $L_2 = 3$, as shown in figure 7(a). The critical Reynolds number and corresponding frequency are computed as $R_c \approx 0.03648$ and $\beta \approx 0.3450$, so we can estimate

$$\check{R}_p \approx p_e^{1/2}(R_c - \check{R}_c/p_e) \approx 15.1502, \quad \check{\beta} \approx p_e^{1/2}\beta \approx 10.9086, \quad (\text{C } 21)$$

for use in making the comparison. The numerically computed eigenfunction has been normalised so that $\max(\Re(\check{q})) = 1$, which occurs at the downstream end of the channel, so in what follows we can set $\Re(\check{q}(1)) = \check{Q}_2(0) = 1$.

The asymptotic prediction of the static membrane profile in region 1 (2) is shown as a line with triangles (open circles) in figure 7(a,i), showing good qualitative agreement with the numerically computed profile (solid line). Furthermore, the asymptotic prediction of the perturbation eigenfunction profiles are shown in figures 7(a,ii) (\check{q}) and (a,iii) (\check{h}), respectively, compared to their numerically computed equivalents.

REFERENCES

- ARMITSTEAD, J.P., BERTRAM, C.D. & JENSEN, O.E. 1996 A study of the bifurcation behaviour of a model of flow through a collapsible tube. *Bull. Math. Biol.* **58** (4), 611–641.
- BERTRAM, C.D. 2003 Experimental studies of collapsible tubes. In *Flow in collapsible tubes and past other highly compliant boundaries* (ed. P. W. Carpenter & T. J. Pedley), pp. 51–65. Kluwer.
- BERTRAM, C.D. & TSCHERRY, J. 2006 The onset of flow-rate limitation and flow-induced oscillations in collapsible tubes. *J. Fluids Struct.* **22**, 1029–1045.
- CANCELLI, C. & PEDLEY, T.J. 1985 A separated-flow model for collapsible-tube oscillations. *J. Fluid Mech.* **157**, 375–404.
- DRAZIN, P.G. & REID, W. H. 1981 *Hydrodynamic Stability*. Cambridge University Press.
- ELAD, D., KAMM, R.D. & SHAPIRO, A.H. 1987 Choking phenomena in a lung-like model. *J. Biomech. Engng.* **109**, 1.
- GAVRIELY, N. & GROETBERG, J.B. 1988 Flow limitation and wheezes in a constant flow and volume lung preparation. *J. Appl. Physiol.* **64** (1), 17–20.
- GAVRIELY, N. & JENSEN, O.E. 1993 Theory and measurements of snores. *J. Appl. Physiol.* **74** (6), 2828–2837.
- GLENDINNING, P. 1994 *Stability, instability and chaos: an introduction to the theory of nonlinear differential equations*. Cambridge University Press.
- GROETBERG, J.B. & JENSEN, O.E. 2004 Biofluid Mechanics in Flexible Tubes. *Ann. Rev. Fluid Mech.* **36**, 121–147.
- HEIL, M. & BOYLE, J. 2010 Self-excited oscillations in three-dimensional collapsible tubes: simulating their onset and large-amplitude oscillations. *J. Fluid Mech.* **652**, 405–426.
- HEIL, M. & HAZEL, A.L. 2011 Fluid-structure interaction in internal physiological flows. *Ann. Rev. Fluid Mech.* **43**, 141–162.
- JENSEN, O.E. 1990 Instabilities of flow in a collapsed tube. *J. Fluid Mech.* **220**, 623–659.
- JENSEN, O.E. 1998 An asymptotic model of viscous flow limitation in a highly collapsed channel. *ASME J. Biomech. Engng.* **120**, 544–546.
- JENSEN, O.E. & HEIL, M. 2003 High-frequency self-excited oscillations in a collapsible-channel flow. *J. Fluid Mech.* **481**, 235–268.
- KECECIOGLU, I., MCCLURKEN, M.E., KAMM, R.D. & SHAPIRO, A.H. 1981 Steady, supercritical flow in collapsible tubes. part 1. experimental observations. *J. Fluid Mech.* **109**, 367–389.
- LIU, H.F., LUO, X.Y. & CAI, Z.X. 2012 Stability and energy budget of pressure-driven collapsible channel flows. *J. Fluid Mech.* **705**, 348–370.
- LIU, H.F., LUO, X.Y., CAI, Z.X. & PEDLEY, T.J. 2009 Sensitivity of unsteady collapsible channel flows to modelling assumptions. *Commun. Numer. Meth. Engng.* **25** (5), 483–504.
- LUO, X.Y., CAI, Z.X., LI, W.G. & PEDLEY, T.J. 2008 The cascade structure of linear instability in collapsible channel flows. *J. Fluid Mech.* **600**, 45–76.
- LUO, X.Y. & PEDLEY, T.J. 1996 A numerical simulation of unsteady flow in a two-dimensional collapsible channel. *J. Fluid Mech.* **314**, 191–225.
- LUO, X.Y. & PEDLEY, T.J. 2000 Multiple solutions and flow limitation in collapsible channel flows. *J. Fluid Mech.* **420**, 301–324.
- MITTAL, R., ERATH, B.D. & PLESNIAK, M.W. 2013 Fluid dynamics of human phonation and speech. *Ann. Rev. Fluid Mech.* **45**, 437–467.
- PEDLEY, T.J. 1992 Longitudinal tension variation in a collapsible channel: a new mechanism for the breakdown of steady flow. *ASME J. Biomech. Engng.* **114**, 60–67.
- PIHLER-PUZOVIĆ, D. & PEDLEY, T. J. 2013 Stability of high-Reynolds-number flow in a collapsible channel. *J. Fluid Mech.* **714**, 536–561.
- REYN, J.W. 1987 Multiple solutions and flow limitation for steady flow through a collapsible tube held open at the ends. *J. Fluid Mech.* **174**, 467–493.
- SIVIGLIA, A. & TOFFOLON, M. 2013 Steady analysis of transcritical flows in collapsible tubes with discontinuous mechanical properties: implications for arteries and veins. *J. Fluid Mech.* **736**, 195–215.
- SIVIGLIA, A & TOFFOLON, M 2014 Multiple states for flow through a collapsible tube with discontinuities. *J. Fluid Mech.* **761**, 105–122.

- STEWART, P.S. 2010 Flow in flexible-walled channels and airways. PhD thesis, University of Nottingham.
- STEWART, P.S., HEIL, M., WATERS, S.L. & JENSEN, O.E. 2010 Sloshing and slamming oscillations in collapsible channel flow. *J. Fluid Mech.* **662**, 288–319.
- STEWART, P.S., JENSEN, O.E. & FOSS, A.J.E. 2014 A Theoretical Model to Allow Prediction of the CSF Pressure From Observations of the Retinal Venous Pulse. *Invest. Ophthalmol. Vis. Sci.* **55** (10), 6319–6323.
- STEWART, P.S., WATERS, S.L. & JENSEN, O.E. 2009 Local and global instabilities of flow in a flexible-walled channel. *Eur. J. Mech. B* **28** (4), 541–557.
- WHITTAKER, R.J. 2015 A shear-relaxation boundary layer near the pinned ends of a buckled elastic-walled tube. *IMA J. Appl. Math.* **80** (6), 1932–1967.
- WHITTAKER, R.J., HEIL, M., JENSEN, O.E. & WATERS, S.L. 2010 Predicting the onset of high-frequency self-excited oscillations in elastic-walled tubes. *Proc. Roy. Soc. A* **466** (2124), 3635–3657.
- XU, F., BILLINGHAM, J. & JENSEN, O.E. 2013 Divergence-driven oscillations in a flexible-channel flow with fixed upstream flux. *J. Fluid Mech.* **723**, 706–733.
- XU, F., BILLINGHAM, J. & JENSEN, O.E. 2014 Resonance-driven oscillations in a flexible-channel flow with fixed upstream flux and a long downstream rigid segment. *J. Fluid Mech.* **746**, 368–404.
- XU, F. & JENSEN, O.E. 2015 A low-order model for slamming in a flexible-channel flow. *Quart. J. Mech. Appl. Math.* **68** (3), 299–319.